



Thermal fatigue and soldering experiments of additively manufactured hot work tool steels

Termisk utmattning och solderingexperiment av additivt tillverkade varmarbetsstål

Henrik Andersson

Faculty of Health, Science and Technology

Degree project for Master of Science in Engineering, Mechanical Engineering

30 hp

Supervisor: Pavel Krakhmalev

Examiner: Jens Bergström

2018-07-04

Abstract

Modern manufacturing processes are under a never ending evolvement. Lowered manufacturing costs, higher part quality, shorter lead times and lower environmental impact are some important drivers for this development. Aluminum die casting is an effective and attractive process when producing components for e.g. the automotive sector. Die casting process development, and hot work tool steel development for the die casting dies has led to the state of the art of die casting today. However, with the disruptive emergence of Additive Manufacturing (AM) of hot work steel alloys, new interesting features such as improved conformal cooling channels inside die casting molds can be produced. The new way to manufacture die casting dies, need basic investigating of the AM produced hot work tool steel properties, and their applicability in this demanding hot work segment.

Die casting dies face several detrimental wear mechanisms during use in production, three of which has been isolated and used for testing three AM produced steel alloys and one conventional premium hot work tool steel. The wear mechanisms simulated are; thermal fatigue, static soldering and agitated soldering. The aim is to study the AM produced steels applicability in the die casting process. The tested materials are; Premium AISI H13 grade Uddeholm Orvar Supreme, AM 1.2709, AM UAB1 and AM H13.

Based on current investigations the conclusion that can be made is that with right chemistry, and right AM processing, conventional material Uddeholm Orvar Supreme still is better than AM H13. This also complies with the literature study results, showing that conventional material still is better than AM material in general.

Sammanfattning

Våra moderna tillverkningsprocesser är under ständig utveckling. Drivande motiv är minskade tillverkningskostnader, högre tillverkningskvalitet, kortade ledtider samt minskad miljöpåfrestning. Pressgjutning av aluminium är en effektiv och attraktiv tillverkningsprocess ofta använd inom till exempel fordonsindustrin. Utvecklingen av pressgjutningsteknologin har gått hand i hand med utvecklingen av det varmarbets-verktygsstål som används i gjutformarna (pressgjutningsverktyget). Den utvecklingen har lett till dagens processnivå och branschstandard. Men med den revolutionerande additiva tillverkningsteknologins (AM) intåg, och möjlighet att producera komponenter av varmarbetsstål, kommer nya intressanta möjligheter att integrera komplex geometri så som yt-parallella kylkanaler i verktyget utan att tillverkningskostnaden blir för hög etc. Det nya sättet att producera pressgjutningsverktyg ger upphov till behovet av grundläggande materialundersökningar av sådant AM-material, samt hur tillförlitligt det är i pressgjutningsverktyg med pressgjutningens krävande materialegenskapsprofil. Pressgjutningsverktyg utsätts för många förslitningsmekanismer och för höga laster, tre av dessa mekanismer har isolerats för kontrollerade tester av ett konventionellt material och tre AM materials responser. Förslitningsmekanismerna som efterliknats är; termisk utmattnings, statisk soldering och agiterad soldering. Målet med undersökningarna är att studera AM producerade materials lämplighet i pressgjutningsprocessen. De material som testats är konventionella premium varmarbetsstålet Uddeholm Orvar Supreme av typ AISI H13, AM 1.2709, AM UAB1 och AM H13.

Undersökningarnas slutsats är att med rätt kemisk sammansättning, och med rätt AM printing parametrar, är konventionellt material fortfarande mer applicerbart i pressgjutning än AM producerat. Den slutsatsen faller väl i samklang med resultaten från mekanisk provning som återspeglas i litteraturstudien, som visade visar att konventionellt material är generellt bättre än AM material

Content

1	Introduction	1
1.1	Aluminum die casting	1
1.2	Hot work tool steel	2
1.3	Additive manufacturing	2
1.3.1	Additive manufacturing process parameters.....	3
1.3.2	Additive manufacturing feedstock powder	4
1.3.3	Additive manufacturing of AISI H13	5
1.4	Mechanical fatigue	7
1.5	Thermal fatigue	9
1.5.1	Thermal fatigue theoretical background	12
1.5.2	Review of temperatures and strains in die casting tooling, and thermal fatigue testing....	14
1.6	Soldering	15
1.6.1	Theoretical background to soldering	17
1.6.2	Connecting soldering mechanisms to binary phase diagrams.....	19
2	Aims.....	22
3	Materials and methods	23
3.1	Test materials	23
3.2	Experimental design	26
3.3	Thermal fatigue	26
3.4	Soldering	28
3.5	Stationary soldering.....	30
3.6	Agitated melt soldering	31
3.7	Evaluation procedures.....	31
3.7.1	Thermal fatigue	31
3.7.2	Static soldering	32
3.7.3	Agitated soldering	33
3.8	Helium gas pycnometry	34
4	Results.....	39

4.1	Thermal fatigue results.....	39
4.2	Static soldering results.....	42
4.2.1	Agitated soldering results	45
5	Discussion.....	46
5.1	Thermal fatigue	47
5.2	Static soldering	50
5.3	Agitated soldering.....	59
5.4	Validity and reproducibility	62
5.5	Future work	63
6	Conclusions	64
7	Acknowledgements.....	66
8	References	67
	Appendix 1.....	71
	Appendix 2.....	72

1 Introduction

This master thesis is based on experimental evaluation and comparison of additive manufacturing (AM)-produced hot work tool steels and conventionally produced reference tool steel used in a specific industrial hot work application, namely die casting. In this section, the reader will be given a comprehensive introduction to the basic corner stones of the work. Firstly aluminum die casting and hot work tool steel are explained.

The dies used in die casting is manufactured from tool steels, and now with the AM revolution the industrial interests arise in adopting this new manufacturing technology in producing the dies. Additive manufacturing and the parameters governing the process will thereafter be explained. An AM specific literature survey on hot work tool steel grade AISI H13 material properties will also be given and compared to a market premium hot work tool steel from the steel producer Uddeholms AB called Uddeholm Orvar Supreme.

In the die casting operation, the die casting mould faces high mechanical loads, high temperature gradients and chemical loads, all acting as detrimental factors, and thereby rendering the mould a finite life. The failure mechanisms studied in the thesis; thermomechanical fatigue and soldering, will be introduced lastly in this section.

1.1 Aluminum die casting

Die casting is a casting method where the molten metal is injected into a permanent mould, or die casting tool made from hot work tool steel at high speed. The production rate as well as part quality is very high, thus attractive from both economic and quality perspective. Many alloys can be die casted, generally materials are split into the subdivision; Zincs, Aluminums and Brasses, where difficulty increases with the succession from Zincs to brasses.

The automotive industry relies heavily on die casting, one estimation from Bonollo et.al (2015) [1] claims that 60% of light material castings in European cars (80-100 kg/car) are die casted components. The development towards using more die casted components, and their increased complexity and difficulty to die cast, gives rise to adopting the new attractive attributes with Additive Manufacturing of die casting molds. Die casting and High Pressure Die Casting (HPDC) are complex processes, and many errors in the castings can occur. In die casting a rather high rejection rate scraps 5-10% of the produced castings, and 5% of the scraped parts is rejected due to the casting/mould interaction errors such as heat checking

markings on the cast part. Heat checking is one type of fatigue wear that the die casting mould suffers from, chemical corrosion and intermetallic layer formation are other detrimental wear mechanisms found in die casting.

Speaking more specifically about aluminum die casting, the aluminum A380 alloy and the hot work tool steel grade AISI H13 is often mentioned in literature, closer discussion on hot work tool steel will follow next.

1.2 Hot work tool steel

Hot work manufacturing processes such as die casting, hot forming, hot shearing, press hardening and forging requires very specialized tooling materials. The tool steels used in this manufacturing segment exhibit excellent; hot hardness, high tempering resistance, toughness and ductility. One of the most widely used hot work tool steel in die casting tooling is the AISI H13 alloy.

Through careful engineering of both chemical composition and microstructure, the hot work tool steels can cope with such property demands. Hot work tool steels are often medium to high carbon steels, and have a fine grained martensitic structure. The hot work tool steels high levels of strength comes from a high dislocation concentration and from the strain the solute carbon exerts on the martensite. After proper heat treatment the tempered martensitic matrix is tough and ductile, and dispersed carbide phase particles with higher hardness increase wear resistance and durability. Principal alloying elements in hot work tool steels are Carbon, Manganese, Molybdenum, Nickel, Chrome, Silicone, Vanadium, Wolfram and Cobalt. As an example on elements function in the alloy; Manganese increase hot cracking properties in the alloy, Silicon increase the yield strength [2].

1.3 Additive manufacturing

Additive manufacturing is generally considered as a new manufacturing paradigm. During the recent years the development has been rapid. Now, an accepted production method, but still, a technology still in its infancy. The AM materials investigated in current report exclusively were produced with the powder bed laser melting method, thus only the laser melting AM process will be presented in the introduction.

In a recent state-of-the-art survey done by Klocke et.al 2017 [3], hot work is described as one of the developing frontiers in the AM field. Many attractive AM attributes such as

manufacturing complex geometry and conformal cooling channels generates a market need for AM hot work materials. However, in AM the processing of hot work alloys has proved to be challenging, and intricate process development is needed. Klocke et.al further state that the high material mechanical property profile demanded in hot work applications, to a great extent is fulfilled by highly refined conventional raw material manufacturing processes, and the new processing technology inherent to AM therefore has to produce like worthy materials in order for hot work material and market process applicability. The processing parameters used in AM manufacturing of the material, therefore intimately correlate with the mechanical properties of the produced material, and hence the AM hot work applicability.

1.3.1 Additive manufacturing process parameters

In the additive manufacturing method Selective Laser Melting (SLM), a laser beam melts selected areas of a powder bed. By traversing the single melt pool on the powder bed, melt track after melt track together form a welded plane or a layer. A re-coater deposits a fresh powder layer upon the previously melted one, and the process repeats. The stacked planes of weld beads form a three dimensional object- the final work piece. Many fundamental and interlinked variables control this delicate process, some concerning the stock powder, some the machine dynamics, and some the laser source. For a comprehensive review the reader is directed to other more prominent scholars on the specific subject, for this present discussion only a basic overview will suffice.

In AM SLM process, all alloy materials need optimized process parameters in order to print components of high quality and mechanical strength. The development is laborious, and non-trivial. The aim is to minimize porosity and cracks in the printed material, and the parameter development is often performed with the aid of statistical Design-of-experiments (DOE) software.

Key AM parameters such as laser input power, scan speed, layer height and laser spot diameter combines to the Volumetric Energy Density (VED). The energy per volume expression is one way to control the AM process, and with the DOE-method porosity can be minimized by altering the VED. The VED-equation is shown below in equation (1).

$$VED = \frac{P}{v * \sigma * t} \left[\frac{J}{mm^3} \right] \quad (1)$$

Where the Volumetric Energy Density, VED [J/mm^3], P = laser input power [Joule], v = Laser scanning speed [mm/s], σ = Laser beam diameter [mm] and t = bed layer thickness [mm], equation referenced from [4].

The volumetric energy density is a general term which is convenient when attempting to describe the energy input into the AM process independent on material, powder or machine. But since the VED is strictly theoretical, without connection to the actual melt pool interaction, and the highly complex physical phenomena who govern the laser/powder melt pool, the use of VED-value parameter have been questioned by some, i.e. [4]. The melt pool interaction with the build plate, the Marangoni heat convection in the melt pool, the vaporized metal recoil pressure and the melt track Plateau-Rayleigh instability are some examples on complex physical phenomena [5], that the VED parameter simply will not capture.

Pores in AM SLM processing generally comes from three sources: the un-melted powder regions called lack of fusion due to too low VED, the gas pores caused by metal vaporization in the melt pool due to too high VED, or hollow powder particles where the trapped gas in the powder particle is trapped in the AM part.

1.3.2 Additive manufacturing feedstock powder

In AM SLM processing, the feedstock raw material is metal powder. Powder feedstock can be produced by gas- and water atomization or centrifugal atomization, where the molten alloy is atomized into a fine powder. For SLM processing Close Coupled Gas Atomization produces the best powder. Many parameters is used in feedstock powder characterization such as particle size distribution, sphericity, aspect ratio, density, tap density, flowability etc. For SLM processing the particle size distribution and flowability are important powder characteristics. Powder particles with trapped atomization gas act detrimental on mechanical and fatigue behavior of AM components, and the entrapped gas cannot completely be removed from the component, not even by Hot Isostatic Press post-treatments. Therefore it is imperative to use high quality feedstock powder in order to ensure the highest possible AM part quality [6].

During AM processing, the un-melted feedstock powder gets recycled for used in future builds. The difference in AM build quality between virgin and recycled powder is a current research topic investigated by many.

1.3.3 Additive manufacturing of AISI H13

Next a comparison of published mechanical properties of conventional AISI H13 and AM H13 will follow. The AM process parameters govern the material properties achieved, and optimizing the parameters is of paramount importance to maximize the material properties. Hot work tool steels are considered as challenging materials to process in AM, process windows are small and sensitive, hence demanding highly refined process parameters in order to yield good material properties. Inherent fault artifacts such as pores, lack of fusion and cracks are responsible for lowering the part density in AM process.

A compilation of reported density measurements of AM processed H13 is shown in Table 1, special attention is directed towards Mazur et.al 2015 reporting as-built densities ranging from 70.53 to 99.99% [7]. The optimization of the build parameters made it possible to reach near maximal density, and thereby enabling reaching high mechanical properties.

Table 1. Compilation of published material density data for AM produced H13 material. Density range from modest 70% to near maximum 99.99% density with optimized process parameters. The rightmost column show conversion to density.

Publication reference	AM-Method	Density [%]	Porosity [%]	Converted to density [%]
[8]	SLM	99.88		99.88
[9]	SLM	>99		>99
[10]	SLM	99.7±0.1		99.7±0.1
[11]	SLM		0.06- 12.74	87.26-99.94
[7]	SLM	70.53-99.99		70.53-99.99

As-built AM H13 material exhibit a microstructure very different from conventional H13, as reported by Yan et.al 2017 [10]. Crystallographic texture, cellular structure and high residual stresses are some of the differences. The residual stresses reported by Yan et.al range between -100 to -1420 MPa compressive stress (ibid). Mazur et.al 2017 [8] report near identical values, and Mertens et.al 2016 [9] found tensile stresses of 375MPa down to -332 MPa dependent on bed pre-heat temperature.

The as-built hardness range widely, and even exceeding the as-quenched hardness level for standard heat treatment of conventional premium H13 material Uddeholm Orvar Supreme. A compilation on published AM H13 as-built hardness is presented in Table 2.

Table 2. Compilation of published as-built AM H13 hardness data. Different sources measured in different hardness units, in the rightmost column the different units are converted to Vickers hardness. As-built AM H13 exceeds the as-quenched conventional Uddeholm Orvar Supreme material.

Publication reference	AM-Method	Hardness unit	Hardness as-built	Hardness heat treated	Converted to HV
[8]	SLM	HRC	59.0 ± 4.6	51.0 ± 3.7	700; 540
[9]	SLM	HV0.5	894 ± 48		894
[12]	SLM	HV	745		745
[13]	SLM	HV5	670		670
[14]	SLM	nanoVickers	748		748
Orv.sup. ref. [15]	CONVENTIONAL	HRC		40-53	390-580

Microstructure influence properties such as tensile yield strength (YS), ultimate tensile strength (UTS) and ductility. Anisotropy in UTS and YS values for AM H13 is reported by both Safka et.al 2016 [12] and Holzweissig et.al 2015 [13]. Both sources report anisotropy depending on the building direction and the layer orientation, this combined renders lower UTS and YS values compared to conventional H13, also ductility is worst in AM H13 since residual stresses and microstructural effects act detrimental.

In die casting tools, the surface topology and finish is important. Safka et.al 2016 [12] made efforts to improve AM H13 as-built surface roughness by adjusting process parameters, and achieved an average surface roughness value of $S_a=21.6\mu\text{m}$. That level of roughness together with as-built topology simply is too rough for the working surfaces of a die casting tool, which calls for post processing of the as-built near net shaped parts from AM processing. Few publications on machining investigations of AM processed materials exists, and only one on AM H13 was found. In this investigation Montevecchi et.al 2016 [16] used the cutting forces in milling as a machinability criterion, comparing AM H13 with conventional H13 material. The findings suggests lower machinability of AM H13 since cutting forces are higher, but since the conventional material was tested in soft annealed

delivery condition and compared with significantly harder AM H13 material, the results and specifically the approach are questionable. In relative terms of machinability, H13 still has a high machinability compared with other tool steels, Uddeholms AB report the machinability of their Orvar Supreme premium H13 tool steel in delivery condition as ~80% to conventional SS2172 plain carbon steel, used for structural applications [17].

In mechanical fatigue tests carried out by Mazur et.al 2017 [8] as-built and stress relieved as-built AM H13 specimens were tested in a rotating bending (R-1 fully reversed load) test rig. As reference conventional H13 material was used. In a Stress-Number to failure (S-N) diagram, AM H13 shows significantly lower fatigue strength. At 1×10^6 cycles conventional H13 had a fatigue limit of ~900MPa, stress relieved as-built AM H13 ~350 MPa and as-built AM H13 ~100 MPa. Internal defects and residual stress act detrimental to fatigue life. However, it should be noted that the AM H13 had as-built surface finish, and the conventional H13 reference was turned. The surface conditions are heavily influential on fatigue performance, thus the test is somewhat ambiguous.

On the subject of AM processed thermomechanical fatigue and soldering behavior, no publications have been found. The only relevant publication discovered in literature was written by Wang et.al 2007 [18]. Work on the evaluated iron-based alloy composition is far from AISI H13, with a chemical composition consisting of 29wt% Ni, 8.3wt% Cu and 1.35wt% P. The authors measured the 15 longest cracks mean crack length, the longest crack, and crack density. The result was then compared with conventional H13 data from other scholars work performed earlier in the same equipment. The conclusion from the tests are that the AM produced material is more prone to cracking than conventional material, and that cracks nucleated at pores, grew along phase boundaries and was likely to follow microstructural irregularities and faults.

To conclude, the authors state that the thermal fatigue resistance of their AM alloy is below that of conventional H13 tested at similar conditions.

1.4 Mechanical fatigue

Before introducing the concept of thermal fatigue, mechanical fatigue will shortly be discussed. Fatigue is the result of cyclic stress imposed on a component. The stress leading to fatigue cracking is lower than the materials yield stress point(YS), but the repetitive

nature of the load nucleates cracks due to the mobility of dislocations, that moves at micro-level even though the bulk material stress level is well below Y_S . The dislocations move in very localized areas near stress concentrations, such as micro cracks, inclusions or pores in the material, and eventually the combined movement results in a nucleation point of a crack. The crack grows with time, and results in catastrophic failure if the load is high enough to propagate the crack, and the fluctuating loads continue.

The relationship between stress level and cycles to failure are called the Wöhler curve or S-N diagram, where the fatigue life is shown as a function of load and cycles. This curve is material specific. The short fatigue life at stresses near the Y_S load limit, are called the low cycle fatigue region. When the load decrease further, the fatigue life is extended, and approaches the fatigue limit and infinite fatigue life. This applies to steel, but the concept of a fatigue limit is heavily debated, since ultrasonic fatigue test running 10^9 cycles and more show that there is no real infinite fatigue life stress level, eventually fatigue cracking happens.

Using material with high cleanliness, low level of inclusions, well-designed components with smooth surfaces and few stress concentration geometries are imperative concepts for avoiding fatigue cracking. Still, fatigue related wear is a very prominent problem in industry, causing high costs annually.

In Figure 1a, an $\varnothing 10\text{mm}$ rotating bending fatigue test specimen fracture surface is shown. The material is the hot work tool steel Uddeholm Orvar Supreme, and the hardness is 48HRC. The fatigue crack started to nucleate at a small slag inclusion of $\varnothing 30\mu\text{m}$, then slowly propagating outwards in a typical “fish-eye” manor $\varnothing 600\mu\text{m}$ (seen in c.). Then when the crack front met the specimen surface, the crack growth sped up, until the remaining material section was too small to carry the load and catastrophic failure occurred (seen in b.). The sample suffered 42.5 million cycles at an alternating 785MPa stress level ($R=-1$), before final rapture occurred.



Figure 1. a) $\varnothing 10\text{mm}$ Uddeholm Orvar Supreme rotating bending fatigue specimen with fatigue fracture in b) and fish-eye nucleation point in c).

1.5 Thermal fatigue

Die casting dies suffer from wear introduced by fatigue mechanisms, which is the main acting deteriorating mechanism [19, 20]. The most common cause of ending a die casting tool's productive life is excessive heat checking, which is leading to gross cracking. Heat checking is an intricate web of surface fatigue cracks caused by the thermal gradients acting on the tool each casting cycle. The small fatigue cracks nucleate in the surface layer, especially at stress concentrating areas or temperature hot spots. The cracks then propagate until either the casting defects caused by heat checking disqualify the cast part surface integrity, or gross cracking causes total tool failure. Corrosion from liquid aluminum on injection mould steel material can cause soldering or washout, and thus acting as stress raisers and crack nucleation sites [21].

In Figure 2., a 300mm die casted aluminum belt pulley from a consumer washing machine are depicted. The pulley is shown in b), where casting defects originating from thermal cracking and heat checking of the mould can be observed on the pulley spokes. In a), one

spoke is depicted with higher magnification, and very pronounced detrimental casting defects can be seen. The cracks in the mould propagates with successive casting cycles, and eventually the mould suffers from gross cracking, or the out-of-spec part quality disqualifies the mould from further use in production. In c) a radius on the pulley show evidence of soldering, observed as a small area with fracture surface (red arrow), and adhered material showing a “galling” pattern (green arrow). This implies that the aluminum soldered to the mould surface in the casting, and that the fracture surface shown on the pulley was produced when the casting was ejected. Washout was not directly observed, but without access to the whole casting system, with inlets and risers etc., one cannot judge if the mould suffered from washout just from this ocular inspection.



Figure 2. Die casted aluminum belt pulley showing casting defects, originating from thermal fatigue cracks in the mould surface. The general view is shown in b), and one of the spokes are enlarged in a), casting defects denoted with blue arrow. In c) evidence of soldering effects are shown, the green arrow show galling, and the red arrow show fracture surface both implying soldering adhesion.

The stress and strains in the tool surface leading to thermal fatigue cracking originates from thermal expansion. The 700 °C hot aluminum melt enters the “cold” tool (approximately 200°C warm) at very high speed. The filling time is fractions of a second, and the thermal shock therefore is of considerable magnitude. The thermal gradient causes thermal expansion of the tool surface, the strains this causes induce high levels of cyclic stress, and fatigue is hereby a strong acting detrimental mechanism. Wang et.al 2009 [18] measured the strains in thermal fatigue testing that led to fatigue cracking, and deduced that upon heating, the material compressive yield strength limit is exceeded. Fatigue cracks start at plastically deformed areas during the cooling regime of the heat cycle, where tensile stress state opens and propagates the cracks.

In Figure 3 a typical thermal fatigue cracks can be seen in a cross section image. The material is AM H13 and the fatigue cracks nucleated at the surface, and propagated inwards. The right crack propagated through a lack-of-fusion pore.

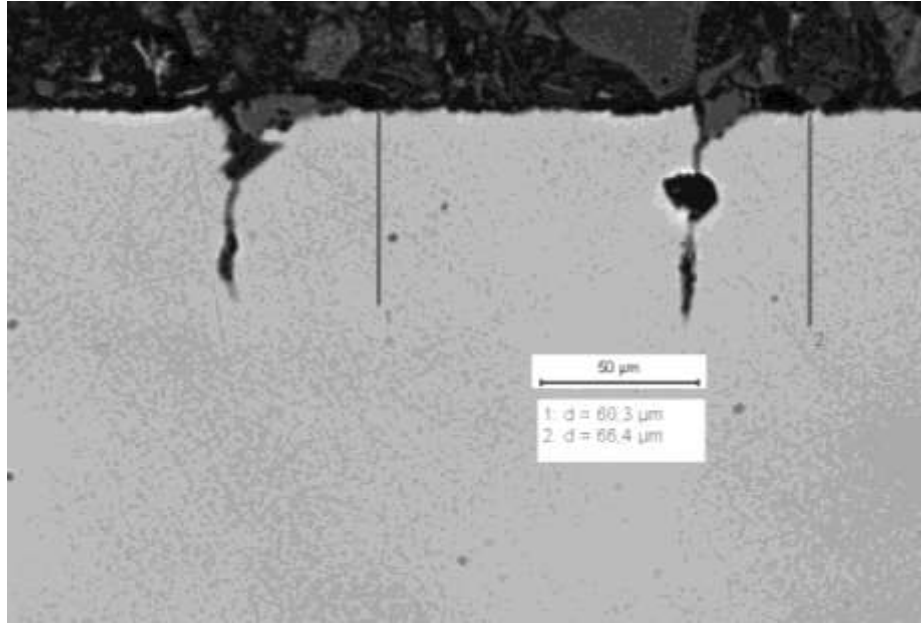


Figure 3. Typical thermal fatigue cracks in AM H13, cross section image at x50 magnification observed in LOM.

1.5.1 Thermal fatigue theoretical background

From classic mechanics theory, the law of thermal expansion and Hookes law with temperature term dictate that change in temperature generates volume change and that strains arise in materials upon temperature change. For a non-constrained body a homogeneous thermal load leads to an expansion and change in length (ΔL), as described in equation (2) [22].

$$\Delta L = L_0 \alpha \Delta T \quad (2)$$

Where; ΔL change in length due to temperature change, L_0 = original length before temperature change, α = coefficient of thermal expansion and ΔT = change in temperature.

The strain caused by the thermal expansion (ϵ) can be described with Hooks law with temperature term, as described by equation (3) [22].

$$\epsilon = \epsilon_{\text{tot}} = \epsilon_{\text{stress}} + \epsilon_{\text{temperature}} = \frac{\sigma}{E} + \alpha \Delta T \quad (3)$$

Where; ϵ = strain, ϵ_{stress} = strain from mechanical load stress, $\epsilon_{\text{temperature}}$ = strain from temperature change, σ = mechanical stress, E = Young's modulus, α = Coefficient of thermal expansion and ΔT = change in temperature.

If idealizing a section of the mould geometry producing the spoke in Figure 2b), we get a geometry similar to the one depicted in Figure 4, which for simplicity can be treated as a beam.

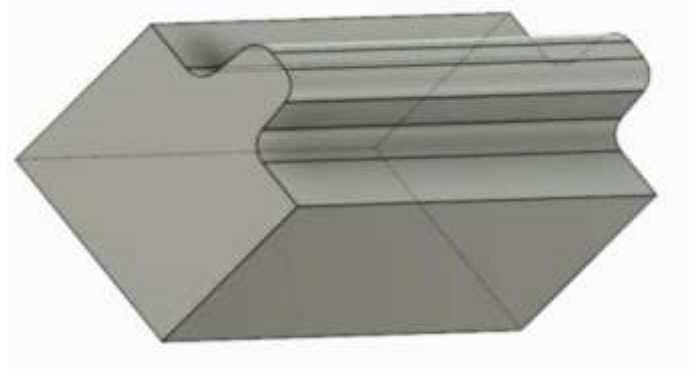


Figure 4. Idealized section of the diecasting die used to produce a belt pulley. Geometry idealized as a beam.

Classical beam theory dictates that non-uniform heat expansion of such beam leads to stress and strain, and as discussed previously cyclic stress and strain lead to fatigue cracking. The protruding top of the beam with the two radii forms the geometry of the pulley spoke, as earlier shown. The cyclic heat from the melt, causes non-homogenous straining of the surface, and fatigue cracking will eventually occur. After cracking and crack growth, the casting defects shown in Figure 2 will become more and more prominent. The stresses that arise in the beam are called “strain-controlled stress”, and can be described with equation 4 below, referenced from [23]. Local heating leads to local expansion, that is resisted by the surrounding material itself, thus “strain-controlled” stress arise.

$$\sigma_m = -\frac{1}{L} \int_{-L/2}^{L/2} E \alpha (T - T_0) dx' = E \alpha \Theta_m (T_0 - T_f) \quad (4)$$

Where; σ_m = membrane stress, L =plate thickness, E = Young's modulus, α =Coefficient of linear expansion, Θ_m =nondimensional mean temperature, T = temperature at X-position, T_0 = original uniform temperature, T_f = face temperature.

1.5.2 Review of temperatures and strains in die casting tooling, and thermal fatigue testing

Practical measurements of temperature profiles in die casting tooling were made by Persson 2003 [24], both Figure 6 and Figure 5 are reproductions from [24]. Thermocouples were placed near the mold surface, and data logging of the temperature change during the casting cycles were done. The recordings are shown in Figure 6, where the temperature as a function of time is shown. The temperature in a typical die casting cycle varies between approximately 200-700 °C. When the temperature curve is used to calculate the stress-time behavior in the mould, Figure 5 can be studied.

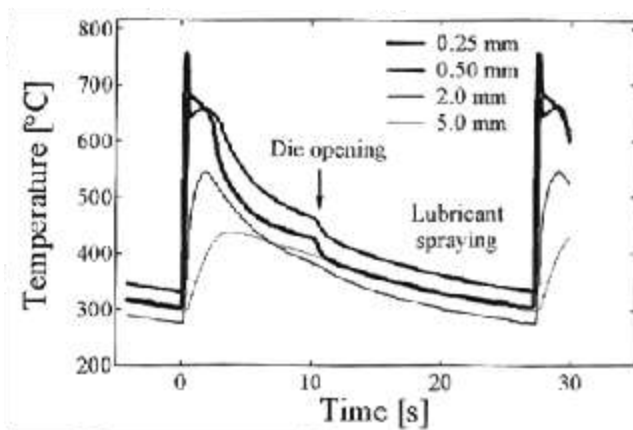


Figure 6. Temperature curves in an aluminum die casting die. Thermocouples were embedded at four different depths from the surface and a casting cycle elapsed. Figure reproduced from Persson 2003, p15.

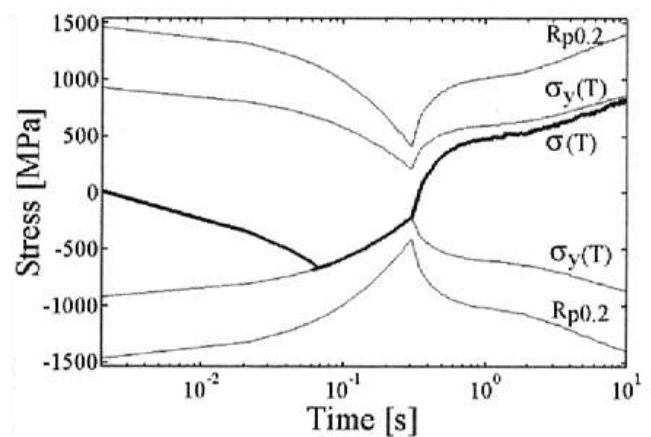


Figure 5. Stress level as a function of time measured in a aluminum die casting tool. Figure reproduced from Persson 2003, p27.

The stress-strain changes during the casting cycle, and eventually cracking occurs. The cyclic strain in a H13 thermal fatigue sample were measured by Sjöström 2004 [25], the results are reproduced in Figure 7. The H13 sample measured strain during fatigue testing, and upon heating the axial and tangential strain exceeds 0.15, and during cooling approaching zero strain. The cyclic straining plasticize the material in compression during heating, the cracks nucleate and grows during cooling.

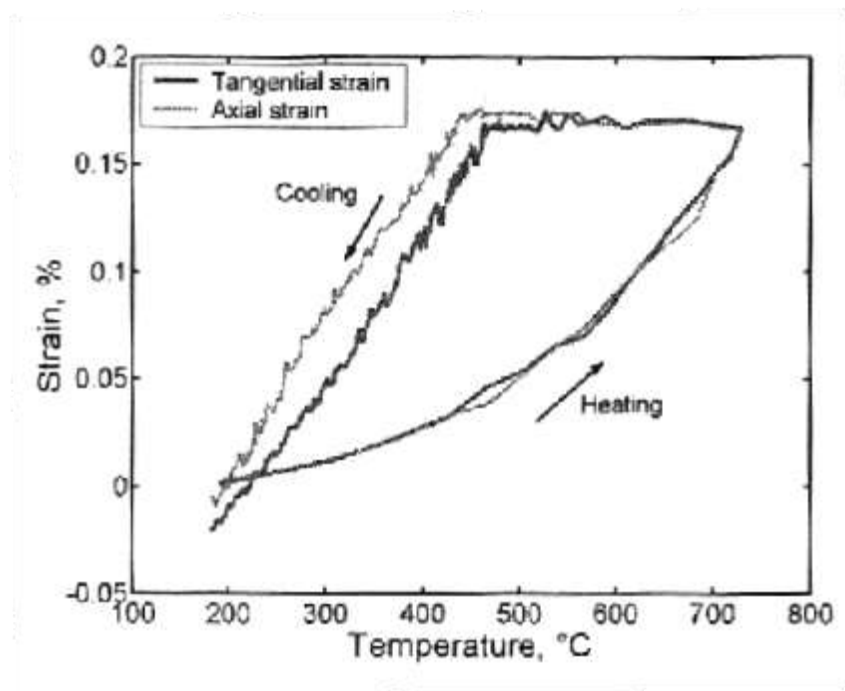


Figure 7. Strain-temperature cycle for a H13 thermal fatigue specimen. Both Tangential and axial directions are shown. Figure reproduced from Sjöström 2004, p33

1.6 Soldering

When molten aluminum inside the die casting mould contacts the hot work tool steel surface, a chemical interaction is started between the liquid and the solid. The aluminum wets the surface, and at the interface chemical interactions take place. The affinity between the materials generates chemical driving forces and potential differences. Intermetallic layers are formed on the tool surface, this mechanism is called soldering. Chemical corrosion at elevated temperature wears the dies. In die casting the very high melt velocities also can cause wear by erosion mechanisms, but in this work only soldering and agitated liquid soldering is investigated. An example of an intermetallic layer formed by molten A380 on an AM UAB1 soldering sample can be studied in Figure 8. Several intermetallic compound layers are formed on the substrate material (bottom). The immersion time was 60min at a temperature of 680°C.

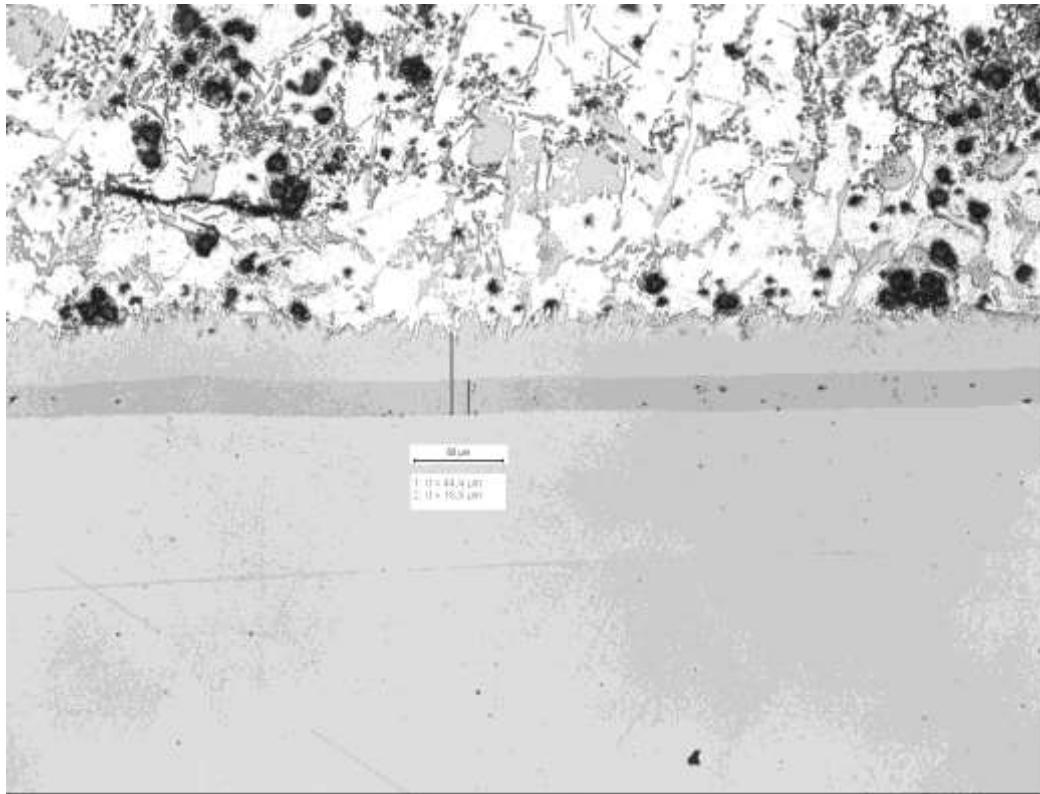


Figure 8. LOM image of a soldered intermetallic layer of A380 on AM UAB 1 soldering sample. Substrate at the bottom, adhered aluminum at the top. The intermetallic layer is the two gray layers in between.

The formation and subsequent growth of the intermetallic compounds are diffusion driven. The temperature and the concentration of elements at the surface determine the growth rate. In H13/aluminum A380 couple, the increase in thickness over time is suggested as parabolic, meaning the layer thickness growth rate are more rapid at first, and declining with increasing layer thickness. Figure 9 show the theoretical parabolic growth rate equation used by Nazari et.al [26] when characterizing the intermetallic growth rate. Plots of three lines with different k-value are shown in the diagram. By fitting the experimental data to this model, a comparison between alloys can be done, by comparing k-, t^a and C-values. The intermetallic growth kinetics can be evaluated and compared between differences in material response with this approach.

The intermetallic growth deteriorates the steel surface. The intermetallics react with the steel, and cause growth, but the intermetallics also react with the aluminum melt and disintegrate. This acts as an active wear mechanism. The intermetallic compound composition in Aluminum A380 and H13 steel are reported by [27] to be $Al_xFe_ySi_z$ combinations. The authors argue that an intermetallic layer can consist of several

compositions of $\text{Al}_x\text{Fe}_y\text{Si}_z$ since thermodynamics enables several compounds to co-exist at the aluminum melting temperature and above.

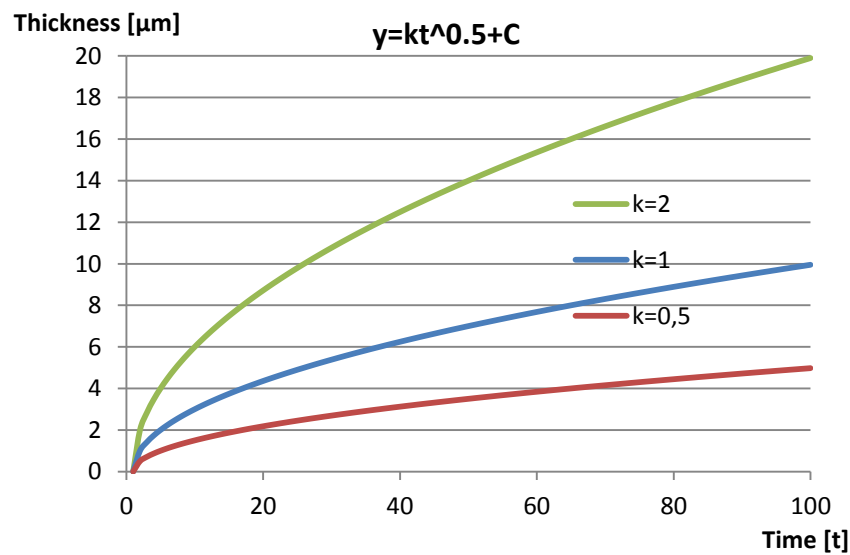


Figure 9. Plot of theoretical parabolic growth rate equation of intermetallic layers.

1.6.1 Theoretical background to soldering

A discussion about soldering will follow. First, a simplification will be made; the H13/A380 couple previously mentioned, will be simplified to Fe-Al couple, and basic interactions will be reviewed. Then the tertiary Fe-Al-Si couple will be mentioned, since it resembles H13/A380 better than only Fe-Al models.

In Figure 10 the binary phase diagram for the Fe-Al alloy can be seen (figure reproduced from Shahverdi et.al 2002 p346 [28]). Temperature is shown on the vertical axis, and atomic- or weight percent Al in Fe from 0% to 100% are shown on the horizontal axis. The areas in the graph shows possible combination of Fe-Al compounds. At the die casting temperature of 700°C, several Fe-Al compounds can coexist.

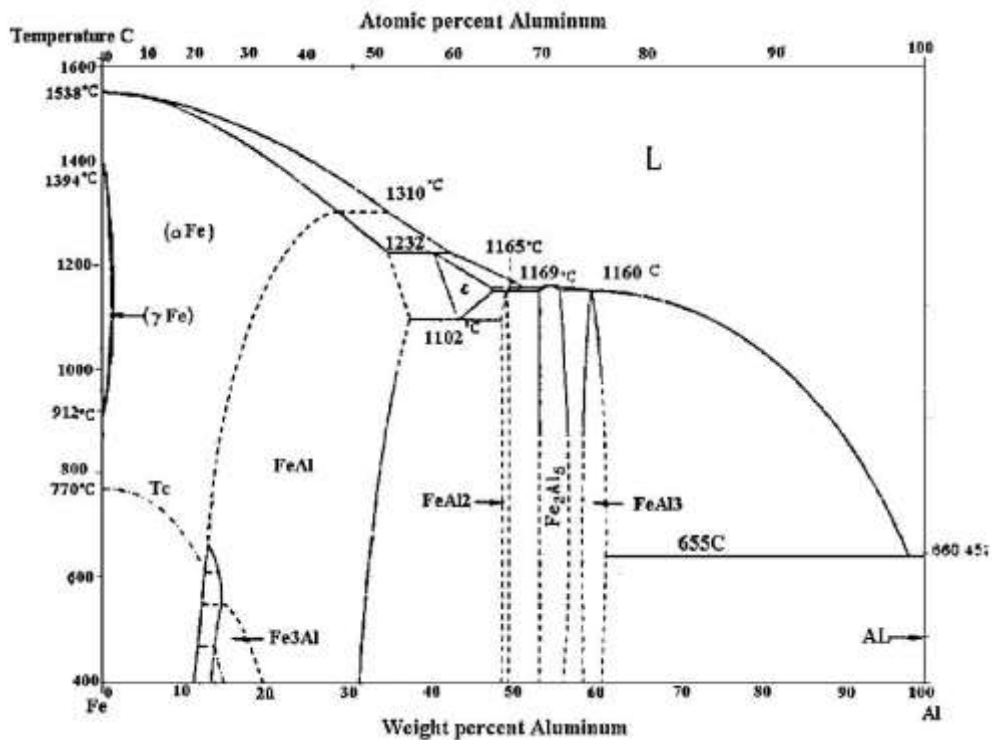


Figure 10. Equilibrium phase diagram for Fe-Al compounds, figure reproduced from Shahverdi et.al 2002 p346.

The different compounds all have different properties, Shahverdi et.al 2002 p346 [28], also show how the compounds respective crystal structure, stability and density. This data is reproduced in Table 3. The compounds have a range of crystal structures, stabilities and densities.

Table 3. Fe-Al phases and their respective crystal structure, stability and density. Reproduced from Shahverdi et.al 2002 p346.

Phases	Crystal structure	Stability range (at.%)	Density (Mg mm^{-3})
Fe solid solution	BCC	0–45	7.8
γ -Fe	FCC	0–1.3	7.8
FeAl (β_2)	BCC (order)	23–55	5.58
Fe ₃ Al (β_1)	Do3	23–34	6.72
Fe ₂ Al ₃ (ϵ)	Cubic (complex)	58–65	–
FeAl ₂ (ζ)	Triclinic	66–66.9	–
Fe ₂ Al ₅ (η)	Orthorhombic	70–73	4.11
FeAl ₃ (θ)	Monoclinic	74.5–76.5	3.9
Al solid solution	FCC	99.998–100	2.69

The different phases grow with different speed, Li et.al [29] state that Fe_2Al_5 Grow the fastest, and that FeAl_2 grow so slow, that it might be difficult to detect, or simply non-existing.

1.6.2 Connecting soldering mechanisms to binary phase diagrams

In Figure 11 from Han & Viswanathan 2003 p.146 [30], soldering mechanism, concentration gradient, temperatures and binary phase diagram are used to describe the mechanics of soldering formation in a Fe-Al couple.

In the bottom left corner the die-melt interface is depicted. The surface of the die is divided into three separate areas; I, II and III. Area I have intimate contact with the aluminum melt, here aluminum diffuse into the die surface and iron dissolves into the melt. The Al concentration in the interphase at area I is greatest of the three areas, and the temperature is locally the largest. Temperature and concentration at the interface is shown in the two graphs above the Die-Melt interface. The two lines marked t_1 and t_2 shows gradients as at different time. Time t_1 is before t_2 , the process is diffusion driven, therefore the evolution of $t_1 \rightarrow t_2$ profiles depends on elapsed time.

In area II the die material has no direct contact with the melt. Here the aluminum concentration is lower than in area I, temperature is lower as well, but still higher than the bulk. Finally, in area III the die substrate material approaches the base alloy composition, with low aluminum content approaching zero and lower temperatures.

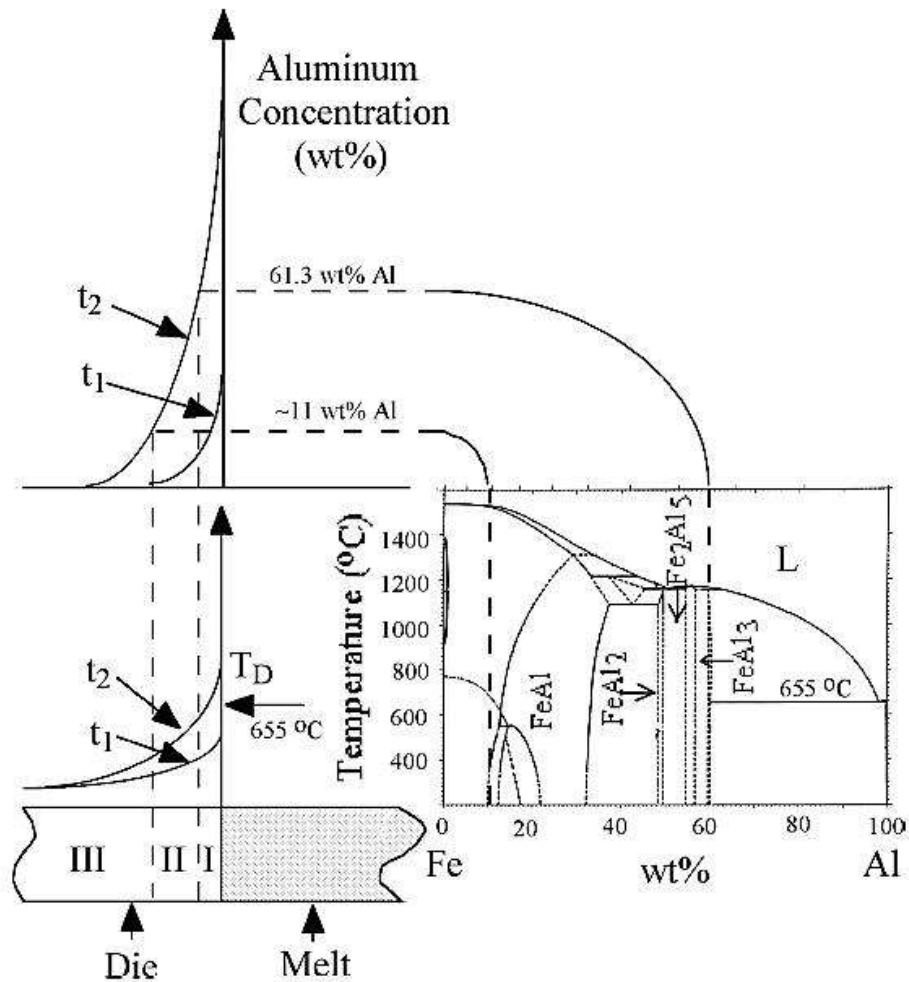


Figure 11. Mechanics and interactions in soldering. The melt/die interface soldering mechanisms are explained with concentration gradients, temperature gradients and binary phase diagram. Reproduced from Han & Viswanathan 2003 p.146.

Intermetallic compounds that can form in the interface are tabulated in Table 4, data referenced from [30].

Table 4. Possible intermetallic compounds in the different areas in a Fe-Al couple interface.

Possible intermetallics	Area I	Area II	Area III
1	FeAl ₃	FeAl ₃	Substrate with > 11 wt% aluminum
2	Aluminum-rich phase	Fe ₂ Al ₅	
3		FeAl ₂	
4		FeAl	

The aluminum concentrations found in area II ranges between 11-61,3 wt%, the dashed lines in the temperature and concentration diagrams shows these limits. Further, the lines extend

into the binary Fe-Al phase diagram. At the temperature range for die casting, this concentration interval can give the intermetallic compounds; FeAl_3 , Fe_2Al_5 , FeAl_2 and FeAl as shown both in the phase diagram and the table.

Die soldering occurs when the interlocking between die and casting in area II is of a certain magnitude. Both the layer thickness and the contact temperature needs to exceed an certain threshold in order for soldering to occur. The mechanical strength of the intermetallic interface is then sufficient to cause adhesive ware in the die [30]

Soldering mechanisms have been explained heavily simplified, with the help of the Fe-Al couple. In a H13-A380 couple a lot more elements than just Fe+Al exists. A380 contains a substantial amount of Si (10,7% as will be shown in Table 8 in coming sections). This makes the interaction and soldering mechanisms more complex. As an example Xiaoxia et.al 2004 [31] show that cast aluminum alloys with high amount of Si retards the diffusion rate of Al in Fe. Slower intermetallic layer growth can be expected in aluminum alloys containing big concentrations of Si.

Expanding the discussion to the ternary Fe-Al-Si system, shown in the phase diagram in Figure 12 , reproduced from [32] p.63, an increase in complexity is found. Depending on the concentration of the compounds at the specific temperature, different phases are present.

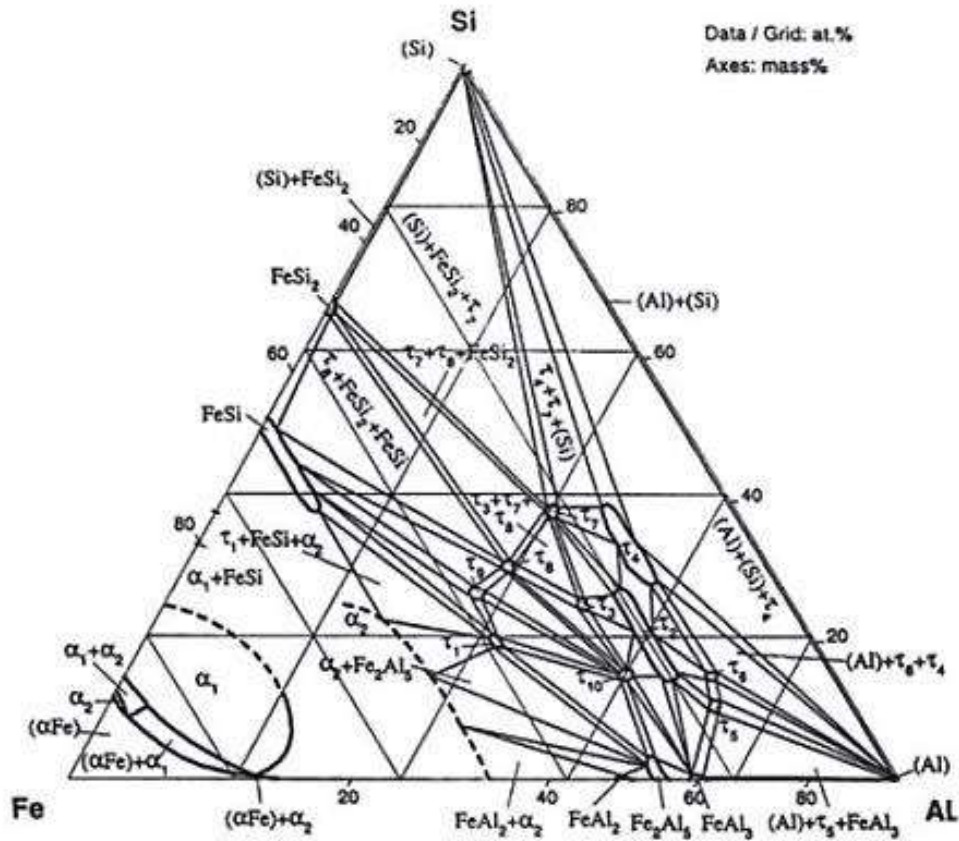


Figure 12. Ternary phase diagram of Fe-Al-Si at 600C, from Mazar et.al p.63.

The concepts from Figure 11 still holds, but is very hard to visualize. Intermetallic compounds form, and chemical gradients exists in the same manor. The interaction and the product of the reactions are complex. Thermo-Calc and DICTRA diffusion simulations can be used to understand the theoretical behavior better. This is not part of current scope, no further discussion will take place here, but suggestions on future work will be given in the “Conclusions ” chapter.

2 Aims

The aims of this master thesis work is to compare AM hot work tool steels against a conventional reference material. Thermal fatigue, soldering and agitated soldering is evaluated via experiments, and conclusions are drawn based on experimental data, whether if AM hot work tool steels can reach conventional tool steel performance, and thus if AM hot work tool steels are applicable in actual hot work tooling applications. Or if further development are needed to enable AM produced tooling to be deployed in industry.

In thermal fatigue the most resilient material based on fewest and shortest cracks is to be determined.

In Static soldering, the parabolic layer growth equation will be used to try to distinguish differences between the materials behavior.

The aim of the agitated soldering experiment is to determine which material has the highest resilience against wear, and if any differences between conventional and AM material can be observed.

3 Materials and methods

In the materials and methods chapter of this thesis, the reader will be given general insight to the test materials, experimental procedure, test equipment and characterization instruments used. The goal is to describe the experimental procedure to the extent where a third party can reproduce the results satisfactorily well.

3.1 Test materials

The test materials investigated in this work can be found in Table 5 below. Basic chemical composition is presented. As conventional reference, Uddeholm Orvar Supreme premium H13 hot work tool steel is used. Three other tool steels are used; AM H13, AM UAB Hot work 1, and AM 1.2709 maraging steel. The developing conceptual alloy AM UAB1's chemical composition are omitted from this review due to Uddeholm AB explicit wish.

Table 5. Basic chemical composition of evaluated materials. All elements in [wt%], rightmost column show the reference to each material composition data.

Material	Fe	C	Si	Mn	Cr	Mo	V	Al	Co	Ni	Ti	Ref.
Orvar Sup	Bal 90,7	0,39	1,0	0,4	5,2	1,4	0,9	-	-	-	-	[15]
AM 1.2709	Bal 64,6	<0,03	<0,1	<0,1	<0,5	4,5	-	0,05	8,5	17	0,6	[33]
AM UAB1	-	-	-	-	-	-	-	-	-	-	-	-
AM H13	Bal 90,53	0,39	0,99	0,3	5,0	1,6	1,13	-	-	0,059	-	XRF

LOM micrographs of polished cross sections of the samples can be seen in Figure 13; Orvar supreme in a), AM 1.2709 in b), AM UAB1 in c) and AM H13 in d). In the left column, polished cross sections can be seen, the magnification is x200, and the inclusions and porosity can easily be seen in the AM-produced materials. Conventional Uddeholm Orvar Supreme shows very few defects, all the AM-materials show pores. Biggest pores exist in AM H13 and AM 1.2709. In the right column, etched micrographs are presented, the magnification is x1000. For Orvar Supreme in a), the fine grained homogenous martensitic grain structure shows well. AM 1.2709 in b), show signs of melt pool lines from printing, so does the AM UAB1. AM H13 in d) have areas that etch white, maybe signs of retained austenite.

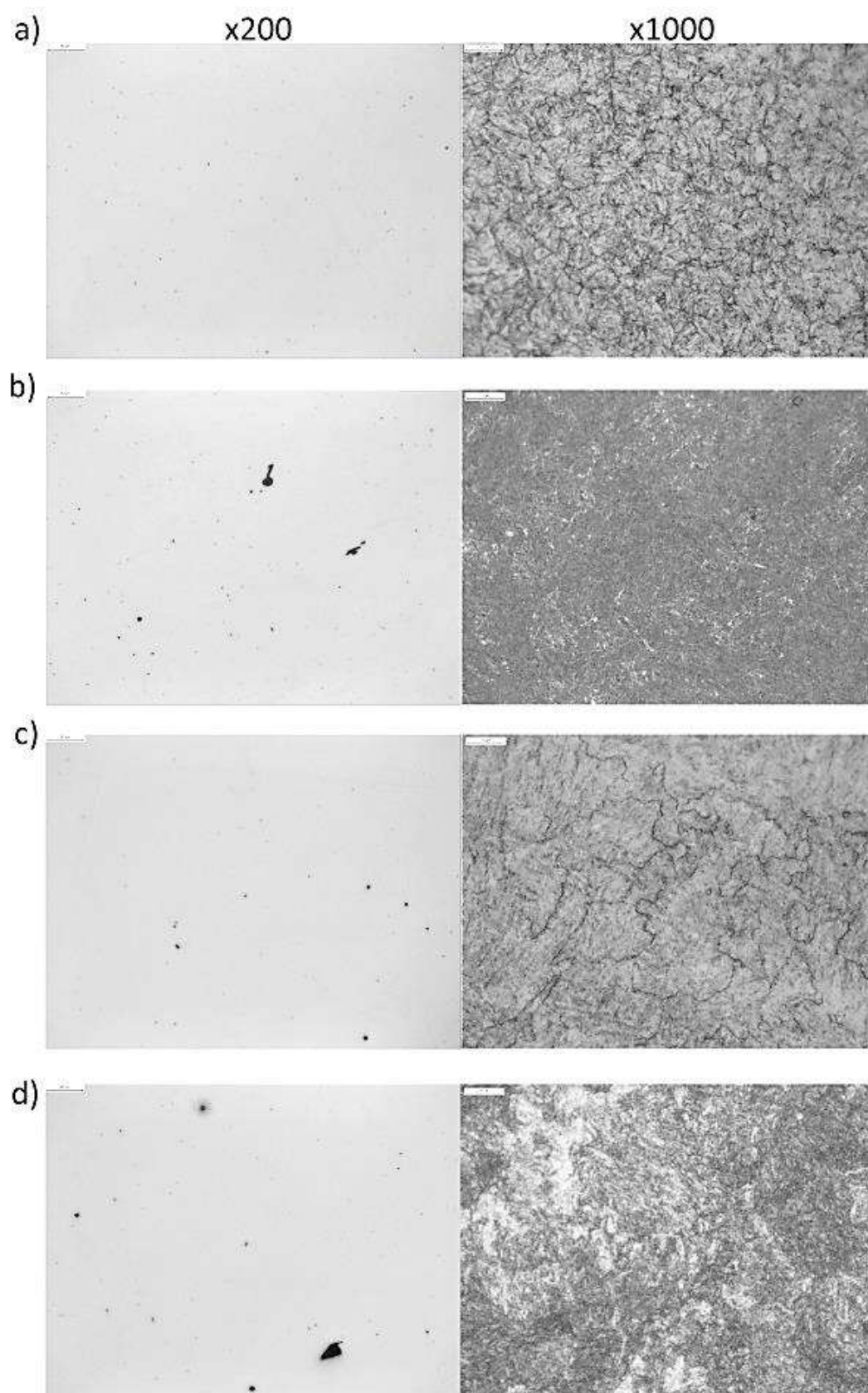


Figure 13. Polished and etched micrographs of the test materials. Polished material in the left column showing porosity, right column with etched specimen show microstructure. Orvar supreme in a), AM 1.2709 in b), AM UAB1 in c) and AM H13 in d).

In Table 6, information on the sample heat treatments and obtained hardness is presented. The aim was to reach 46-48 HRC hardness, a range often used in die casting.

Table 6. Hardness and heat treatment for the test materials used in the work.

	Material	Hardness [HRC]	Heat treatment
1	Uddeholm Orvar Supreme	47,4	1020°C 60min + 580°C 120min x2
2	AM 1.2709	47	860°C 90min + 590°C 180min
3	AM UAB1	46,8	630°C 120min x2
4	AM H13	46,8	1050°C 60min + 600°C 120min x2

3.2 Experimental design

Hot work applicability and relative comparison of AM hot work tool steel versus conventional tool steel is investigated with the following experimental design. Three experiments will be conducted; Thermal fatigue, Static soldering and Agitated soldering. The experimental data will be analyzed, and weighted in order to decide how the different alloy performance compare to each other. In Table 7, a summary of the experimental matrix are presented. The abbreviation for each material is presented in the table, as a key for the reader to understand the coming presentation of the results. In static and agitated soldering one sample per material was used. In Thermal fatigue two samples per material were used.

Table 7. Experimental matrix, with the four test materials, the three test methods, and the abbreviation for each group of samples (S1, A1 etc)

Material	Test		
	Static soldering	Agitated soldering	Thermal fatigue
Uddeholm Orv. Sup.	S1	A1	T1
AM 1.2709	S2	A2	T2
AM Uddeholm 1	S3	A3	T3
AM H13	S4	A4	T4

3.3 Thermal fatigue

The thermal fatigue experiments were conducted at the material testing laboratory at Karlstad University. The same equipment has previously been used in thermal fatigue investigations performed by [18, 24, 25, 34].

The thermal fatigue sample mounted in the induction heating machine (HF-Teknik AB 25kW ME250B) is depicted in Figure 14, the assembly components are marked with balloons.

Sample (1) geometry is a fine centerless ground 80mm long, $\varnothing 10$ mm diameter bar, with a concentric $\varnothing 4$ mm internal cooling channel (see sample manufacturing drawing in appendix 1). A $\varnothing 0,13$ mm K-type thermocouple (6) is spot welded to the sample center, depicted as red and blue wires in Figure 14. The induction cycles applied by the copper coil (4) rapidly heats the sample to maximum preset temperature controlled by the thermocouple, then the sample is cooled by a controlled ramp down of the induction power. Argon shielding gas is flowing inside the orifice (5) formed by the sample and a quartz tube (3) with the aid of two Teflon bushings (2). The temperature curve was calibrated to closely resemble the temperature profile used in the work by Persson 2003 [24], which is based on actual in-situ die casting temperature measurements. The maximum 700°C top temperature is close to the aluminum A380 die casting processing temperature, and the low 200°C temperature is the “bulk idle temperature” the tool is kept at in diecasting to avoid excessive thermal chock. The testing was performed to try to simulate thermal events in die casting of A380 alloy.

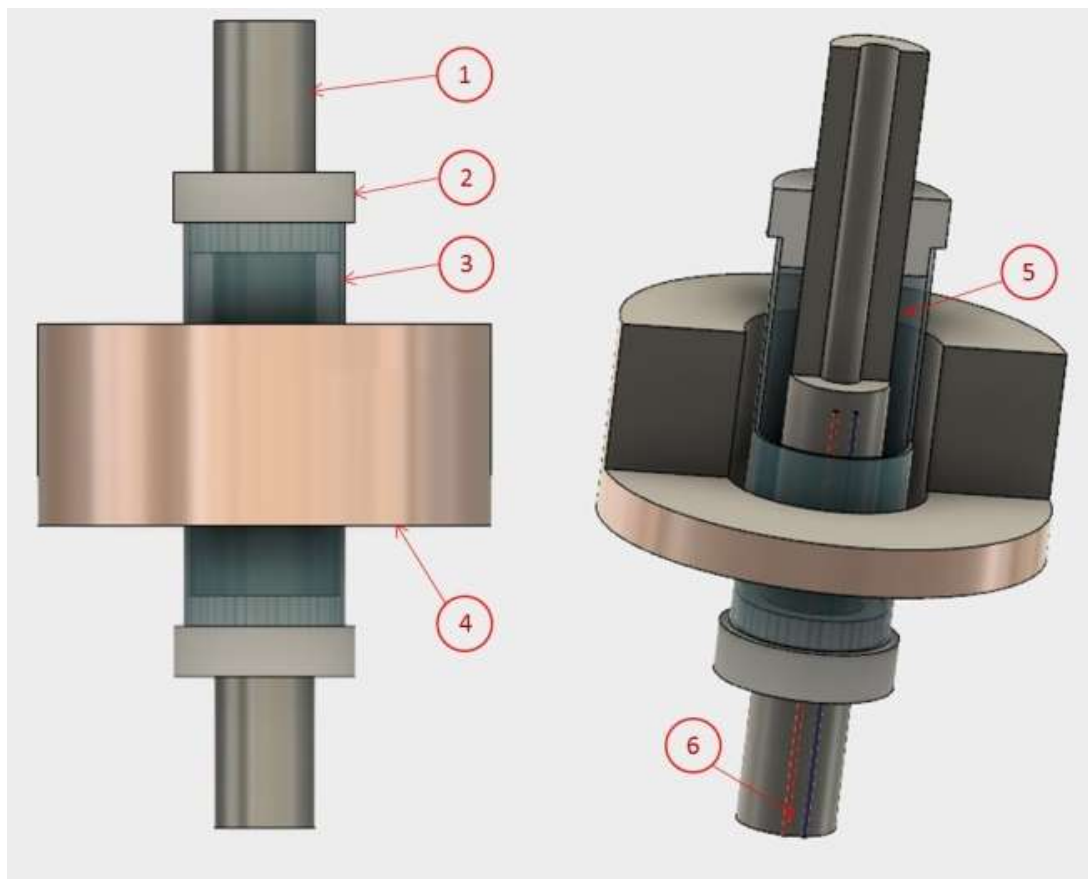


Figure 14. Schematic view of the thermal fatigue setup. Left view shows the intact set up. The right view show a partial cross section of the components in the setup. Components marked with balloons are: 1) Sample, 2) Teflon bushings, 3) Quartz tube, 4) Induction coil, 5) orifice, 6) K-type thermocouple.

The typical temperature cycle can be seen in Figure 15, the maximum temperature is reached in approx. 450ms, and then a forced cool down inside the cooling channel with ~18°C cooling fluid down to 200°C follows, before next cycle starts again. This creates the thermal expansion gradient and stress-strain that ultimately leads to fatigue cracking. Comparing to the measurements of the real die casting process, the temperature in the testing is not as rapid in heating, and shorter than a complete die casting cycle. The testing will be of an accelerated testing type.

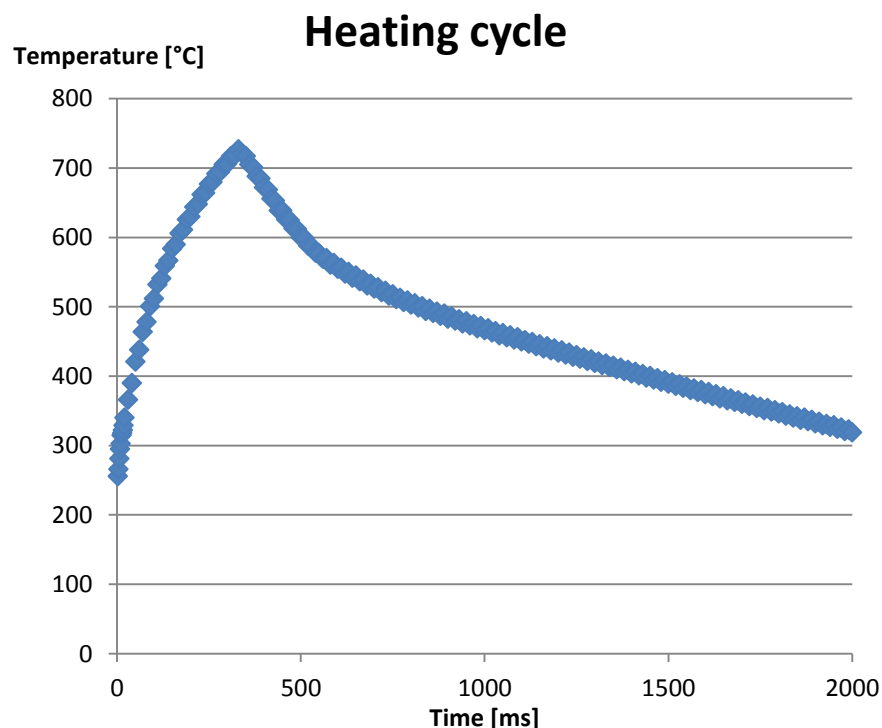


Figure 15. Typical thermal fatigue heating cycle. The diagram show temperature as a function of elapsed time, measured with a spot welded thermocouple on the sample surface.

3.4 Soldering

In this work, the classic die casting alloy aluminum A380 grade are used as die casting aluminum test material. The chemical composition of the test alloy is presented in Table 8 where a chemical analysis of the actual material used is tabulated.

Table 8. Chemical composition analysis of A380 alloy used in soldering tests. Analysis made with XRF-technique. Some detected “exotic” trace elements were omitted from this table.

Al wt%	Si wt%	Fe wt%	Mn wt%	Zn wt%	Cu wt%	Cr wt%	Ti wt%
88,1	10,7	0,81	0,208	0,07	0,05	0,007	0,006

The experimental setup can be seen schematically in Figure 16. The resistance oven used to melt the A380 aluminum, and the sample holder is depicted in Figure 17. The ceramic crucible holds approximately 2,8 kilogram melt. Detailed sample dimensions are shown in appendix 2. The molten aluminum was held at 680°C during all experiments. The PID temperature controller manage to hold the temperature at $680 \pm 10^\circ\text{C}$. Further on, the soldering experiments was split into two parts; stationary soldering and agitated melt soldering.



Figure 17. Temperature controlled Nabertherm resistance furnace and soldering setup with fixtures and holders.

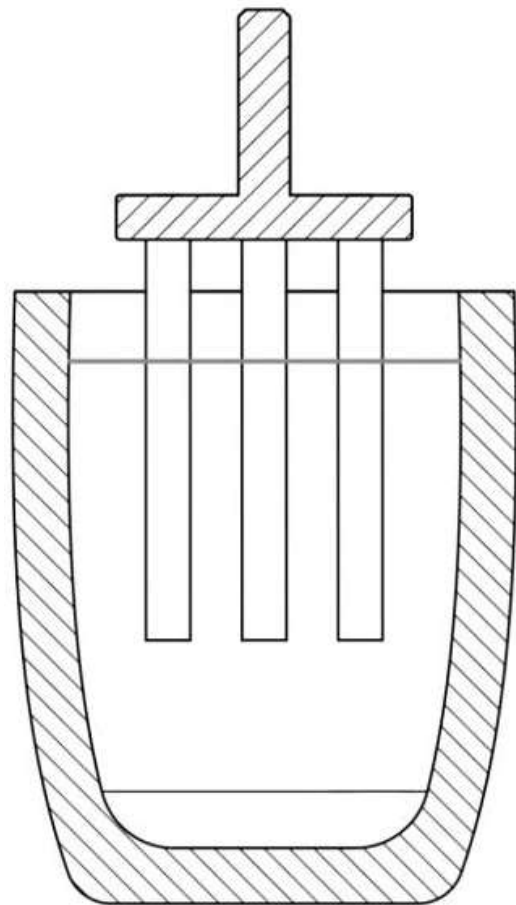


Figure 16. Schematic cross section of the soldering experimental setup. The sample holder and samples are immersed in the aluminum melt inside the crucible.

3.5 Stationary soldering

In stationary soldering, the sample contacts the melt without any relative movement. The liquid melt reacts with the solid steel sample at the solid/liquid interphase. The sample was submerged in to the melt to an immersion depth of 80mm. Then the samples were removed at predetermined time intervals. Between each dipping interval, a 20mm cut-off from the sample bottom was made. With this technique the holding time for each cut off is increasing with elapsing time. The intermetallic layer thickness as a function of time, its growth kinetics and composition can hereby be determined. The procedure and holding times are described visually in Figure 18, the cut off piece marked with one is cut after certain elapsed time, than after further immersion piece two is cut and so on.

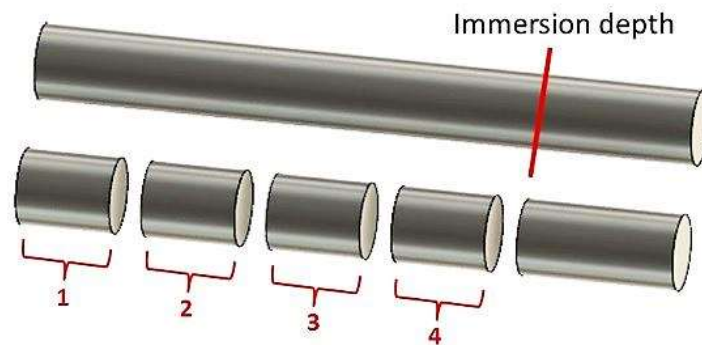


Figure 18. Schematic depiction of stationary soldering experiment. A sample is immersed to the marked immersion depth, held for certain time then removed from the bath. A piece is cut off, and the sample is immersed again which repeats for all four tests and holding times.

The time intervals, holding times and total time for each section is better described below in Table 9. Since the material above experiences multiple submersions, both the interval and the total holding time for each section described in Figure 18 are shown.

Table 9. The immersion times and intervals for stationary soldering samples. Section 1 was cut off after a total holding time of 2min, section 4 was cut off after $2+6+12+40=60$ min total immersion.

Specimen section no.	1	2	3	4
Holding time interval	2 min	6 min	12 min	40 min
Total holding time	2 min	8 min	20 min	60 min

3.6 Agitated melt soldering

In die casting, the melt is injected into the mould at high speed. The impinging liquid can cause erosion like wear mechanisms, but also chemical wash out mechanisms. This occurs at velocities much higher than can be achieved with the current crucible setup (typical injection velocities reach 40-60m/s according to Chen et.al 1999 [35]). Hence the relative velocity of the melt and sample is significantly below ranges that true erosion and wash out occurs. According to this definition, not erosion but agitated melt soldering was used to determine the wear and weight loss caused by the aluminum-steel reaction. The samples were submerged into the crucible, and spun around at 200 rpm (equivalent to approx. 30m/min= 0,5m/s velocity) for 2 hours. 200 rpm was the highest possible velocity tolerated by the current setup. Higher velocities could not be reached because the aluminum melt would have splashed over the crucible, furnace and laboratory floor.

Material weight loss caused by the agitated soldering corrosion was measured with a novel helium gas pycnometry metrology method. The loss of mass, were used as a wear criterion to compare the resistance to agitated soldering performance for the different materials.

3.7 Evaluation procedures

Several evaluation methods were utilized for material characterization. Each of the three experiment evaluation techniques will be described in next coming sections accordingly.

3.7.1 Thermal fatigue

The thermal fatigue samples were inspected visually at low magnification under light microscope (LOM). An image of the sample free surface was recorded at 1,5x magnification. Then a Struers precision discotom of model "Secotom-50" were used to cut the heat affected part of the sample, then the cut of were split down the axial center, principally shown in Figure 19, where the blue area are the evaluated surface. The orientation of the cut was always placed with the thermocouple weldment to the left in the figure. The affected area 90° from the weldment was studied, since the distance from the thermocouple is the same for both of the surfaces depicted in Figure 19. The discotom abrasive cutting disc kerf width was compensated for, to enable a cut down the exact half plane of the cylinder. An 0.2mm allowance for the succeeding polishing step was added to the cut, this makes sure that the evaluated cross sections is very close to the exact half plane as practically possible.

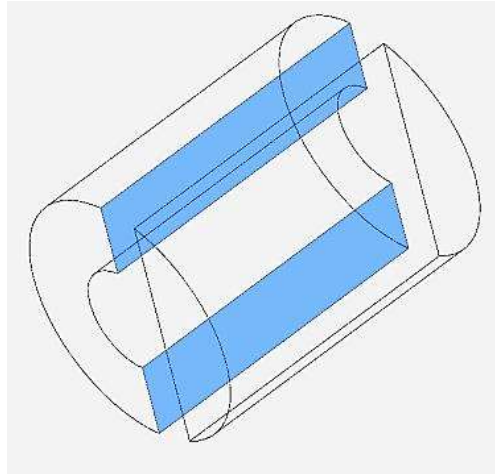


Figure 19. Principe of thermal fatigue sample cross section. The width of the abrasive cutting disc was compensated for, to allow for the blue surface to align to the cylinder half plane

The sample was mounted in a Struers PolyFast Phenolic thermosetting resin in a Struers Citopress-30 machine. Then metallurgical grinding and polishing was performed with the following process sequence: Flat grinding on 400 grit stone, 5min on 9 μ m diamond suspension, 5min on 3 μ m diamond suspension followed by a final 30 second polishing with 1 μ m diamond suspension.

After sample preparation, LOM again were used in order to investigate the affected zone. Cracks were manually processed in a Zeiss Axio Scope A.1 LOM with imaging processing software. The crack length was measured perpendicular to the sample surface. Both sides were measured along the entire heat affected zone length.

3.7.2 Static soldering

The static soldering specimens was processed and prepared in the same grinding/polishing manor as described for thermal fatigue. The cross section is schematically described in Figure 20, the blue surface is the investigated and evaluated area on the sample.

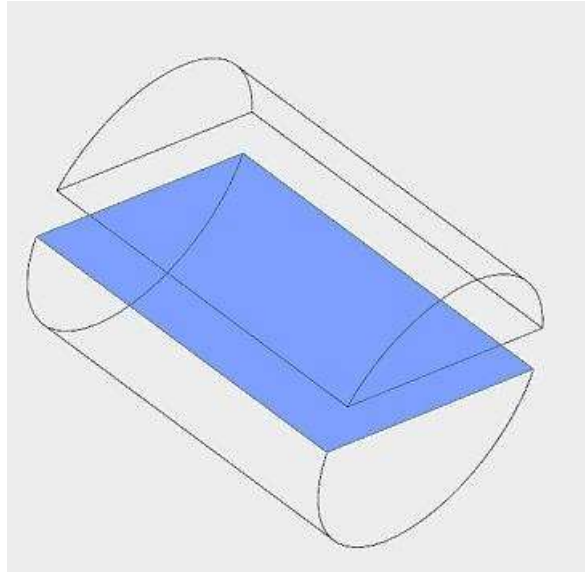


Figure 20. Principe of static soldering cross section. The width of the abrasive cutting disc was compensated for, to allow for the blue surface to align to the cylinder half plane

For static soldering, the intermetallic layer thickness was measured with the Zeiss Axio Scope A.1 LOM. Intermetallic compounds were further analyzed with EDS analysis in SEM, in order to quantify how elements in the intermetallic reaction is distributed.

3.7.3 Agitated soldering

The agitated soldering experiments causes wear of the sample. The amount of worn material after a certain time of exposure, is a measure of the material wear resilience in molten aluminum contact.

Figure 21 show cross sections of agitated soldering samples schematically; a) unaffected sample, b) worn sample with aluminum residue (marked blue) and c) worn sample with removed aluminum layer. By weighing the unaffected sample before and after soldering, the wear can be presented as weight loss per time unit. Before weighing the worn sample depicted in c), the adhered aluminum layer seen in b) has to be removed.

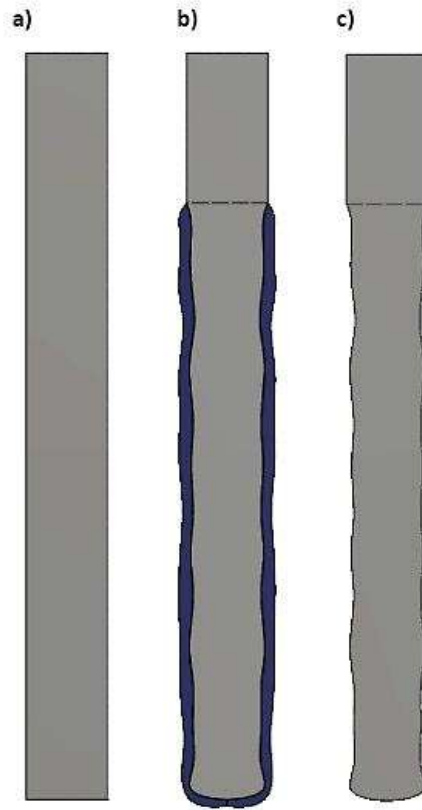


Figure 21. Schematic cross section view of agitated soldering samples. a) showing unaffected sample, b) worn sample with aluminum residue and c) worn sample with aluminum removed

Authors of earlier works used concentrated NaOH-solution [36] or KOH-solution [35] to remove soldered aluminum from the sample surface. Wear can be calculated as material loss by weighing the sample mass before and after soldering. The method is both laborious and time consuming, as well as hazardous and environmentally unfriendly. Novel method development efforts for using helium gas pycnometry, instead of removing aluminum layers with the NaOH-method are next described.

3.8 Helium gas pycnometry

The agitated soldering experiments were evaluated by the use of a helium gas pycnometry instrument of model “Ultrapyc 1200e”. A method was developed to measure the material loss during agitated soldering experiments, where the steel mass is decreased over time, and a certain amount of aluminum freezes on the sample surface (as depicted in Figure 21).

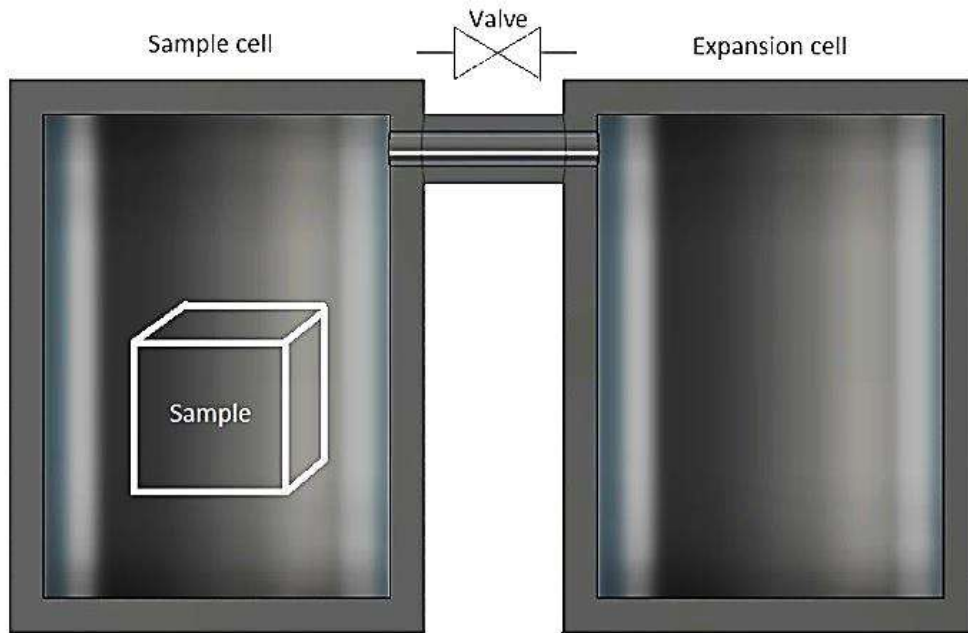


Figure 22. Schematics of pycnometry. A sample is placed in the Sample cell. The empty expansion cell is to the right. The cells are connected via a valve restricted passage. After purging the system with helium, a 19 [psig] gas pressure is applied to the expansion cell. The pressure is equalized after opening the interconnecting valve, and the resultant pressure is in proportion to the displaced volume caused by the sample body.

Next a presentation on the methodology development is given, a schematic view of pycnometry can be seen in Figure 22. In helium gas pycnometry the sample volume; V_{sample} , is precisely measured, and the sample mass is carefully weighed on a balance, then the density is calculated by equation 5. The volume measurement is based on the ideal gas law; difference in pressure between two interconnected compartments called cells is measured at constant temperature. The sample is placed in the first cell, the system is purged with helium gas, and temperature is adjusted to a certain interval. A valve between the cells is closed, and the second cell (called expansion cell) is pressurized with helium. At the preferred pressure (19 [psig]), the interconnecting valve is opened, and pressure is equalized. The sample displaces volume in the measurement sample cell, thus meaning that the equalized pressure is higher compared with the calibrated pressure with empty cells. The change in pressure is then used to calculate the sample volume V_{sample} , according to equation (6), from reference [37].

Density is calculated by the fundamental and classic equation (5):

$$\rho = \frac{m}{V} \quad \left[\frac{\text{g}}{\text{cm}^3} \right] \quad (5)$$

Where: density ρ = [g/cm³], sample mass m =[g] and sample volume V =[cm³].

Sample volume is calculated by equation (6):

$$V_{\text{sample}} = V_{\text{sample cell}} \frac{V_{\text{expansion cell}}}{\left(\frac{P_r}{P_f} \right) - 1} \quad [\text{cm}^3] \quad (6)$$

Where; volume of the sample V_{sample} [cm³], volumes of the measurement cells $V_{\text{sample cell}}$ and $V_{\text{expansion cell}}$ [cm³], cell pressure before equalizing P_r and final pressure after equalizing P_f [psig].

Pycnometry offers density measurements with high accuracy, small deviations and fast and easy handling. Viana et.al 2002 [37] shows that density measurements within 0,01g/cm³ precision can be obtained with the method, and argues that the technique can be used to detect very small changes in density. In the field of minerology, pycnometry has been used to accurately measure the concentration of iron (Fe) in hematite ore. Couto et.al 2012 [38] describes their metrology, and the further method development mentioned below, are based on the idea that pycnometry of the combined density of composites can be used to estimate the mass of individual elements of the composite mixture. For soldering wear evolution, the pycnometry method has not been reported before to the author's best knowledge. The method development efforts are motivated by fast and accurate results and health and environmental safety gains compared to the conventional chemical NaOH-dissolution procedure.

In Figure 23, combined density of A380 aluminum and H13 steel is described. At the diagram main Y-axis, pure H13 density at 7,78g/cm³ act as starting point for the blue line spanning to the secondary Y-axis with A380 density. The line between the Y-axes show combined density as a function of percent A380 in H13. By the lever rule, a measured combined density strictly follows the concentration of A380 in H13. This mean, that the concentration K , in an unknown soldering sample can be calculated via the expression found in equation (7).

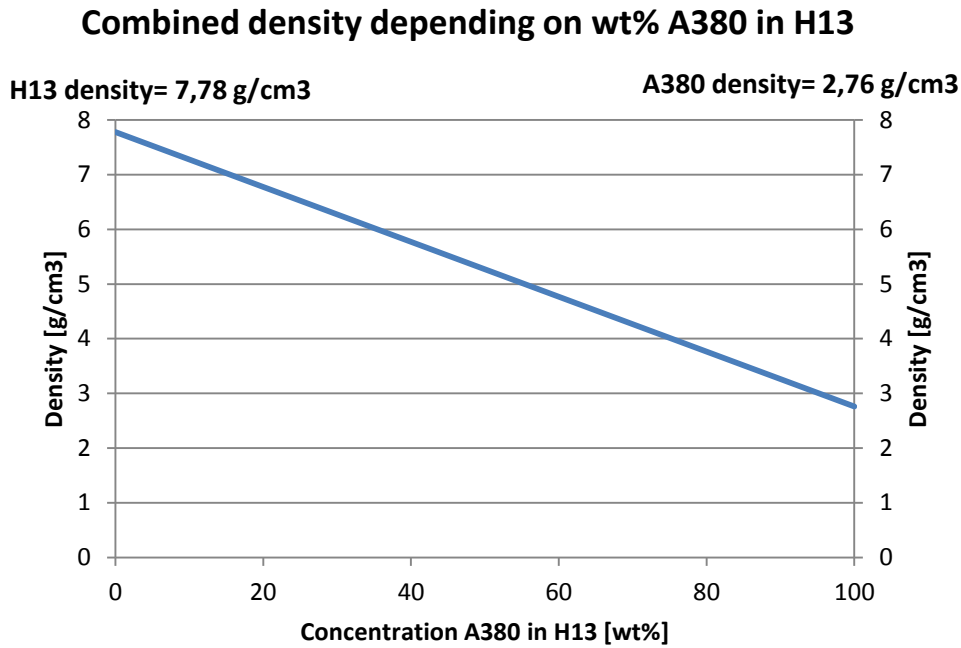


Figure 23. Diagram showing combined density as a function of concentration of A380 in H13. At 0% A380 concentration, the density is the nominal H13 density, and with increasing A380 composition the combined density decreases linearly to the A380 nominal density.

Concentration of A380 on a H13 combined density measurement calculated by:

$$K = -\rho_A * \frac{\rho^* - \rho_s}{\rho_s} [\%] \quad (7)$$

Where; Concentration K [%], ρ_A = density A380, ρ^* = combined density and ρ_s = density H13 [g/cm³].

A soldering sample with the appearance of b) in Figure 21, will strictly show a lower combined density than pure H13, but higher combined density than A380. The concentration A380 is calculated with the formula above, and by weighing the total weight m^* , the weight H13 in the sample can be determined via equation (8).

$$ms = m^*(1 - K) \text{ [g]} \quad (8)$$

Where; m_s = Mass H13 steel [g], m^* = sample total weight [g] and K = concentration factor A380 in H13 [%]

The worn volume can then finally be calculated by knowing the initial sample mass (state a) in Figure 21) by using equation (9).

$$Q = \frac{(m_0 - m_s)}{\rho_s} [\text{cm}^3] \quad (9)$$

Where; Q = the worn volume [cm^3], m_0 = initial sample mass [g] m_s = mass H13 steel [g] and ρ_s = density H13 [g/cm^3].

To test the methodology, and compare the new approach to the conventional NaOH-procedure, various size standards of H13 and A380 were manufactured by turning and grinding to close tolerances and fine surface finishes. The standards volume were calculated by trivial cylinder volume formulas, by measuring geometry with calipers and weighing the standards mass carefully with a high precision balance. Respective material density was calculated, and found to be in close agreement compared with tabulated density values. After these manual density calculations, the gas pycnometer was used to repeat the process. The calculated and the measured density for the materials was found to differ $0.03 \text{ g}/\text{cm}^3$, combined density could then be both calculated and measured. These values also agree to a satisfactory precision for the purposed application.

After successfully measuring the “simulated” H13 worn volume by using combinations of the standards depicted in Figure 24, density measurements and calculations on an actual soldered sample was performed. The combined mass was weighted on a precision balance, the combined density was measured via pycnometry, then the H13 and the A380 mass were calculated. First via pycnometry, than via the NaOH-procedure for the same sample. The metrology was deemed to work with satisfactory precision for the intended use in evaluating agitated soldering.



Figure 24. Standards manufactured in A380 and H13 for pycnometry calibration. The surfaces and edges were carefully machined to fine finish.

The developed equations were used to build an excel spread sheet to speed up the calculation process. One example of such spread sheet will be shown in the coming agitated soldering results section called "5.3 Agitated soldering".

An advantage when using pycnometry over NaOH dissolution, is the un-destructive testing procedure obtained with pycnometry. After density measurements and calculations on wear, the sample can possibly be cross-sectioned for micrographic and microstructural analysis. This would not be possible with NaOH-dissolution since the interesting layer with the experimental information is removed.

4 Results

The results from the experimental work will generally be summated in this section.

Presentation of detailed results from each material and testing procedure will be given in the sections thereafter, one for each test.

4.1 Thermal fatigue results

After the fatigue testing (20k heating cycles) all the free surfaces of the samples were studied in LOM. In Figure 25 the differences in oxide layers can be seen, where T2 AM 1.2709 show heavy oxidation, compared to the other samples. The flow rate of protective argon inert atmosphere was held constant during all tests at 1l/min flow rate.

From ocular inspection of the free surface, it was found that different materials crack differently. The biggest cracks and heat checking was often times found at the edges of the heat affected zone. In sample T2 (AM1.2709 material) heavy oxidation makes it difficult to observe cracks, since the oxide might hide the cracks them self.

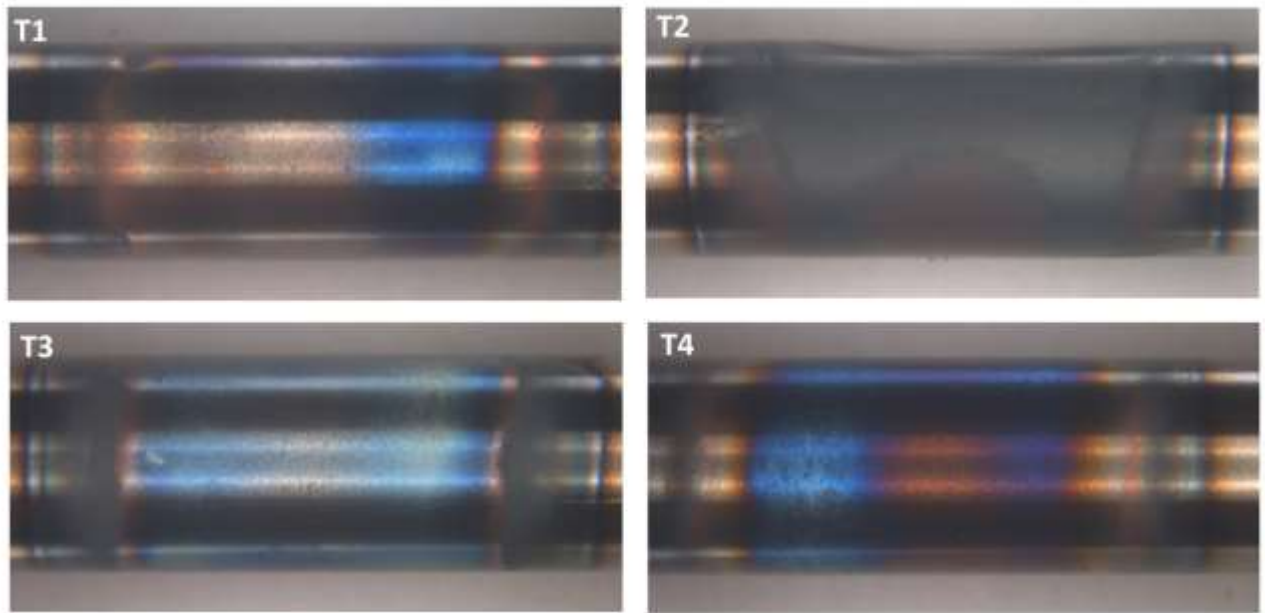


Figure 25. Free surface LOM images of TF samples, one from each material. The oxide layers differ in thickness between the samples, which highlights the heat affected zones. Uddeholm Orvar Supreme in T1), AM 1.2709 in T2), AM UAB1 in T3) and AM H13 in T4).

After ocular inspection the thermal fatigue specimens were cut as described in Figure 19, mounted in thermosetting resin and polished as described in earlier discussion about experimental procedure. The sample cross-sections were then studied in Light Optical Microscope (LOM) at 200x magnification, and the cracks in the heat affected area were measured with the help of image analysis tools.

A micrograph showing typical thermal fatigue cracks are shown in Figure 26. In A), a thermal crack in AM H13 is shown. The crack seems to have propagated through a pore from the printing process (Seen halfway down in the image as a black area). In b) AM 1.2709 show a typical fatigue crack. Both printed materials show signs of porosity. The fatigue cracks both on free surface and cross sections correspond very well to the appearance of cracks reported by [24, 25, 34].

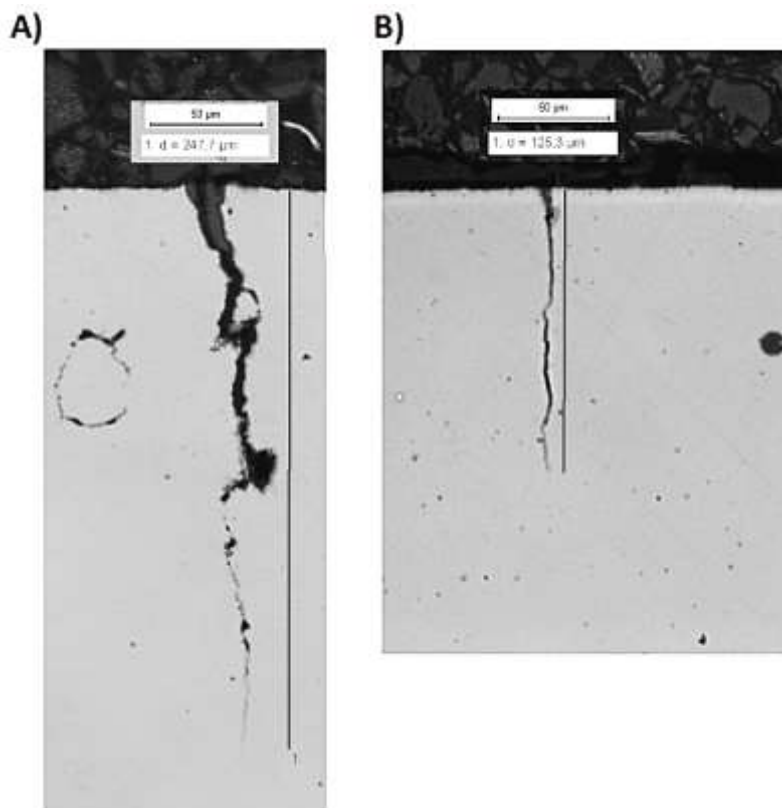


Figure 26. Micrographs of two thermal fatigue cracks at x200 magnification. In A) the crack at midway, seems to have propagated through a pore in the material, then continued its growth.

In these micrographs, it's also pedagogical to show how the crack length was measured. The crack length was measured perpendicular to the surface down to the crack tip, but in some instances the cracks were not as perpendicular to the surface as the cracks shown in the micrographs. A more correct term, maybe, would be to use "Crack Depth" instead of length, since the angle of propagation would lead to a longer diagonal crack length, than just the perpendicular length alone.

All cracks were then compiled in the following histograms showed in Figure 27. The crack lengths were compiled into bin and frequency, than plotted in bar graphs in Excel. Uddeholm Orvar Supreme is plotted in a), AM 1.2709 in b), AM UAB1 in c) and AM H13 in d). AM 1.2709 show largest amounts of short cracks, AM UAB1 show fewest cracks over all. Uddeholm Orvar Supreme show fewer cracks than AM H13. The bin intervals are showing greater detail at shallow cracks, since the frequency of small cracks were dominant.

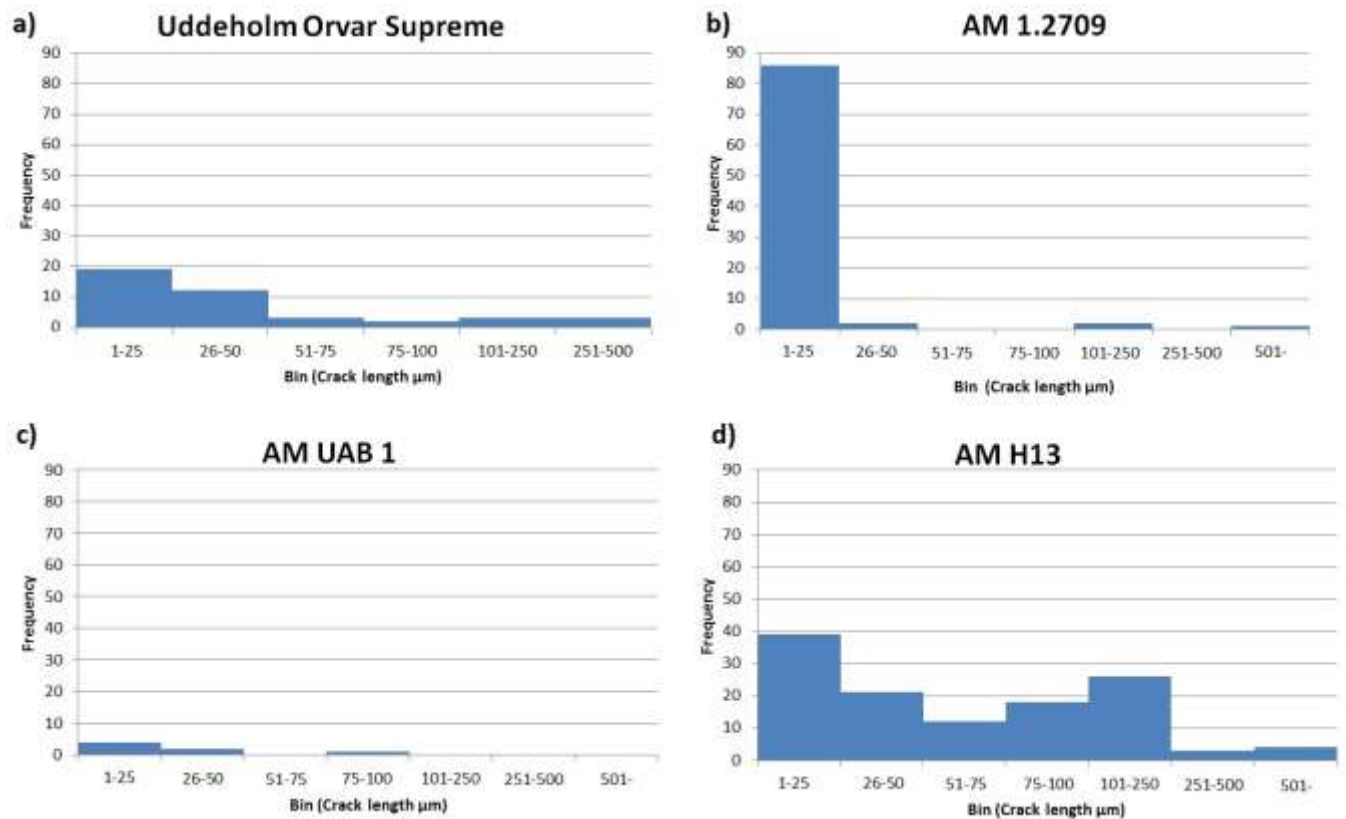


Figure 27. Thermal crack histogram for all measured cracks in two samples of Uddeholm Orvar Supreme in a), AM 1.2709 in b), AM UAB1 in c) and AM H13 in d). The X-axis show the bin interval lengths and the Y-axis show the frequency.

4.2 Static soldering results

In this section results from the static soldering experimental run will be presented.

The experiment was carried out as earlier described. After submerging in the A380 melt, the samples were removed and cut. The process repeated until all four holding times were finished. The cut-offs then were split, mounted in resin and then polished with the polishing procedure earlier described.

The intermetallic layer for each sample was then studied in LOM. The intermetallic layer thickness was measured with image analysis software, and an image was saved on the computer. All the images of intermetallic layers then were compiled into Figure 28, where the test materials S1-4 are shown. One cross section for each time interval is presented. The steel substrate is situated in the bottom of the images, the intermetallic layer in the middle,

adhered A380 aluminum is the white area, and in some images the heavy black structure at the top is the phenolic mounting resin.

In A) Uddeholm Orvar Supreme is shown. Up until 20 minutes the layers seems rather equal, but the 20 minute sample and especially the 60 minute sample show a double layer possibly containing different intermetallic compounds, since the layer closet to the substrate steel have a different shade of gray. This hold true for AM UAB1(S3) and AM H13(S4) as well. For AM 1.2709 (B) only one layer seem to exist, which by far also is the thickest.

In the B) image after two minutes, no layer was formed. The A380 aluminum residue after soldering had not adhered to the surface and simply fell off when the discotom was used to split the sample.

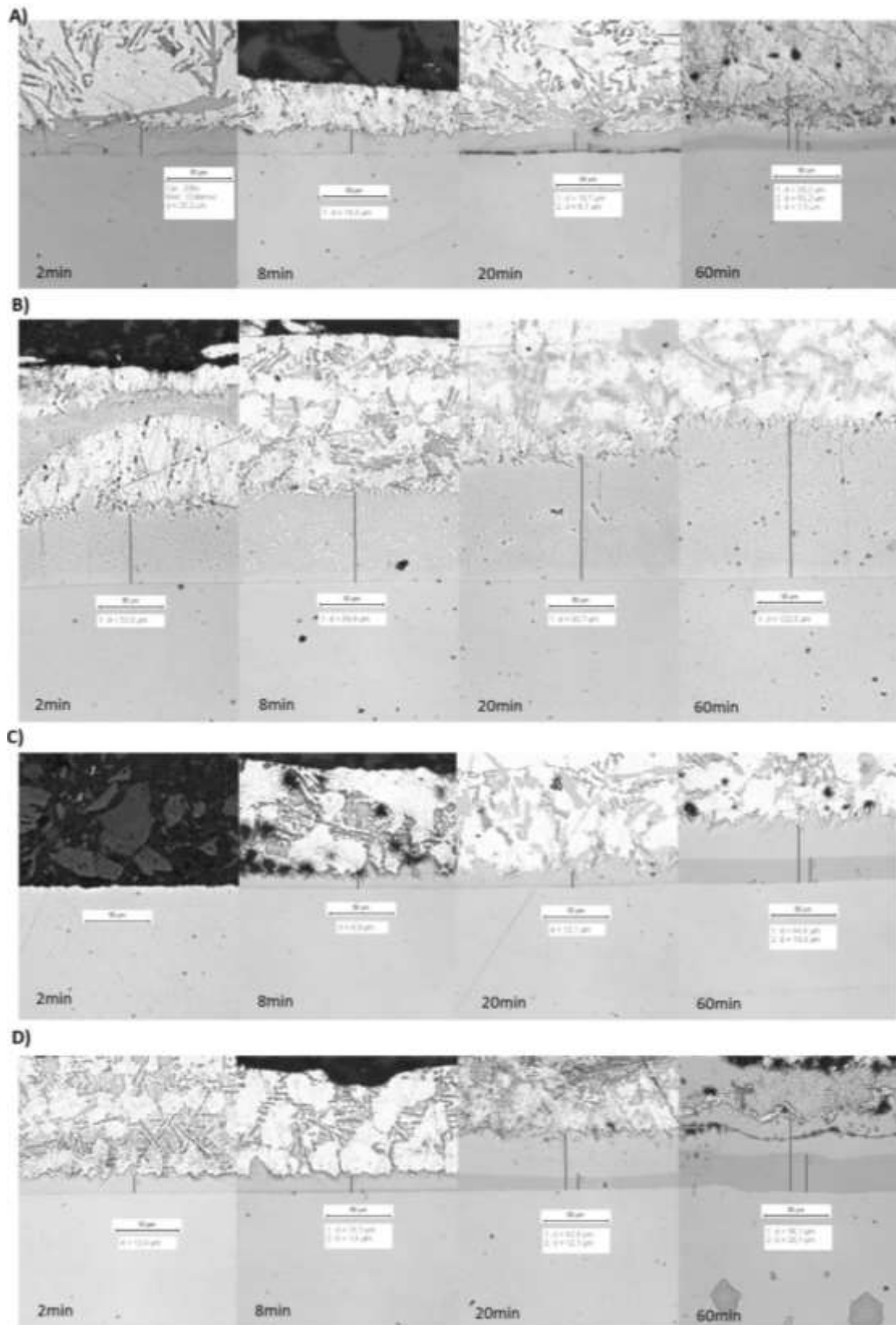


Figure 28. Static soldering experiments, steel substrate at the bottom, adhered aluminum on the top, intermetallic layers in between. A) show material S1 intermetallic layer as a function of time. B) show material S2 and C)-D) show S3-S4 respectively. The 20 and 60 minute layers for all samples except S2 in b) show a two layer structure. For S2 only one layer can be seen. Images taken with LOM at x200 magnification.

The intermetallic layer thickness for each sample was recorded, then compiled in Table 10. Measured intermetallic layer thickness for each material (S1-S4) at different time interval.

Table 10. Measured intermetallic layer thickness for each material (S1-S4) at different time interval.

Layer thickness [μm]				
Time [min]	S1	S2	S3	S4
0	0	0	0	0
2	24,49	53,6	0	12,4
8	18,8	69,9	9,9	13,1
20	16,7	93,7	12,1	42,9
60	20,2	122,5	44,4	56,1

4.2.1 Agitated soldering results

The other kind of soldering experiment- the agitated soldering experiment result will be presented in this section. The samples were submerged into the liquid aluminum crucible and spun around at 200 rpm for 2 hours holding time. The samples were covered in adhered A380 aluminum melt, as shown in Figure 29. After the experiment the samples went through rigorous cleaning in technical alcohol to remove any loose residue from experimental processing.



Figure 29. Agitated soldering specimen after two hours soldering. The material is AM UAB1, and the adhered aluminum can be seen. The big lump in the right of the image was facing the forward direction of rotation inside the melt.

The wear caused by the agitated soldering was determined with the aid of the developed pycnometry methodology. The mass loss for each material is presented in Figure 30 below. The mass loss for A2 (AM 1.2709) is significantly larger than for the other three materials. The difference between A1, A3 and A4 is rather small.

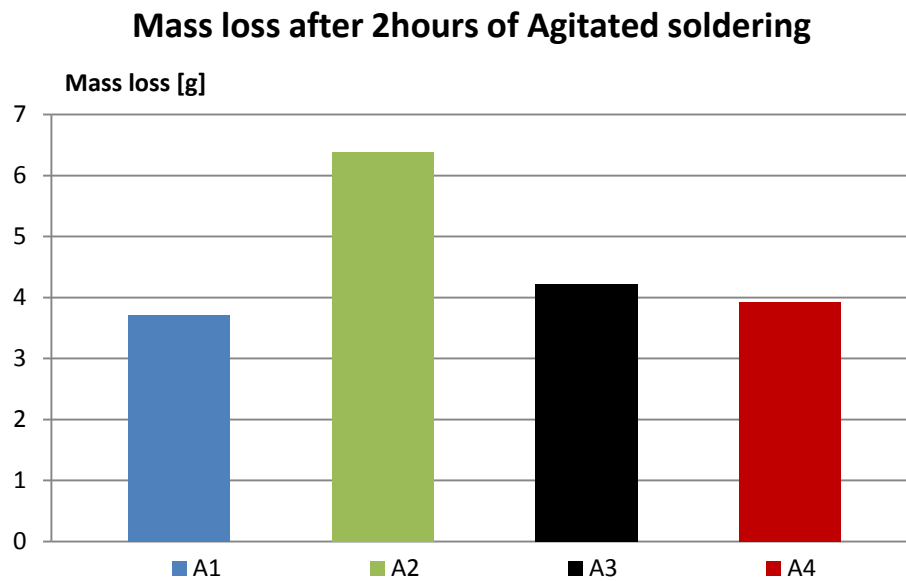


Figure 30. Mass loss for the agitated soldering experiment. The mass loss in gram [g] is shown on Y-axis for each material (A1-A4) shown in the legend. Material A2 suffered from bigger mass loss than the other three materials in the test.

5 Discussion

In this section the results will firstly be summarized in a top-level way. In order to rank the material behavior in each testing method and process this data un-biased, criterion weighting matrixes was used. For thermal fatigue two factors was used; number of cracks, and total crack length. In static soldering the two parabolic rate parameters “K” and “t^a” were used to weight the material response. For agitated soldering, weight loss was used as response parameter. In all weighting low score mean resilient material. I.e. ranking the materials after of the total number of cracks 1-4, and giving the material with fewest crack 1 point, and the material with most cracks 4 points. The two scores for total number of cracks, and total crack length was then added to each other, and became the materials total score for thermal fatigue. The weighting scores for all three experiments were summed up, and the materials were arranged in ascending order with respect to total score. This is shown in Table 11. The most resilient material overall was found to be conventional Uddeholm Orvar Supreme, closely followed by the AM UAB1 conceptual alloy. In split third are AM H13 and AM 1.2709.

Table 11. Result matrix for the test materials 1-4 and their respective scores in Thermal fatigue, Static soldering and Agitated soldering. The total score rank the material performance in accordance to the rightmost part of the table.

Material	Therm.F	Static	Agitated	Total	Rank
1	13	10	1	24	1
2	13	20	16	49	3
3	2	17	9	28	2
4	32	13	4	49	3

→

Rank	Material
1	Orvar Supreme
2	AM UAB 1
3	AM H13
3	AM 1.2709

From an applicability perspective, Uddeholm Orvar Supreme is confirmed to be a very good material choice for die casting applications. Among the three tested AM materials, AM UAB1 is deemed the best choice for die casting applications based on test results. Further on in the results section, detailed results and discussion on each test will be presented.

5.1 Thermal fatigue

The results from thermal fatigue are tabulated in Table 12, where each test material and the total number of recorded cracks and the total crack length are shown. The measured values of total number of cracks and total crack length were summarized in the table. The rank and the weight of each material response to thermal fatigue are also presented (see Table 12). In the weighing, few cracks and short total crack length renders a low weighting score. The lower the score- the better the materials is deemed to withstand thermal Fatigue.

Table 12. Thermal fatigue result, showing each materials number of cracks and mean crack length.

ID	No. Cracks mean	Score	Weight	S*W	tot. Crack l.	Score	Weight	S*W	tot. Score
T1	11	2	2	4	568,2	3	3	9	13
T2	23	3	3	9	370,0	2	2	4	13
T3	2	1	1	1	44,9	1	1	1	2
T4	31	4	4	16	2613,2	4	4	16	32

The AM UAB1 got the lowest thermal fatigue score, since the alloy showed very few cracks, and the crack length was short. This alloy contains higher amounts of Mn (exact amounts are omitted from the discussion due to Uddeholms explicit wish), compared to Orvar Supreme and AM H13. The heat checking resistance is reported by [2] to be closely interlinked with the Mn content. This statement holds true for the two AM hot work grades, but the thermal

fatigue for conventional Orvar Supreme was much better than for AM H13, also the AM 1.2709 performed better than AM H13 even though AM 1.2709 has much less Mn content. But the thermal fatigue and heat checking properties are not dependent on only Mn content; microstructure, homogeneity, porosity and segregation is a few examples in influential factors affecting thermal fatigue resistance [20].

None of the literature references on AM produced H13 tool steel reviewed in the literature study tested thermal fatigue of AM H13. Wang et.al 2009 [18] tested a laser sintered material, but the special work material and the immature AM processing technology used at the time makes it difficult to compare with other work. The findings of Wang were that conventional material was superior to the AM-material. The current investigations show how the conventional Orvar Supreme indeed outperforms the AM H13 material, and the AM 1.2709. But, the AM UAB 1 is better than both Orvar Supreme and AM H13 in the current thermal fatigue test.

The reviewed work on AM H13 and fatigue by [7], suggest that the high level of porosity in the AM H13 thermal fatigue samples in current work acted detrimental to thermal fatigue resistance, and that AM UAB 1 with few observed pores (high density) was more resilient.

In the state-of-the-art survey by Klocke et.al 2017 [3], hot work tool steel alloys for AM were reported to be requested in the market, Klocke's observation on the market need for an AM hot work tool steel have led to that the AM 1.2709 alloy were commercialized as a tool steel, which resulted in that some end users tried to use it in hot work applications. In the current investigations it was shown that the AM 1.2709 alloy exhibit poor chemical resistance in the simulated die casting soldering experiments. The applicability for AM 1.2709 in hot work is poor, but good for the conceptual AM UAB 1 alloy. This means if the company experimenting with this alloy releases it on the market, Klocke's request will be answered.

Based on the thermal fatigue behavior measured in current work, the resilience to thermal cracking of AM UAB1 is equal or even better than conventional Orvar supreme, thus implying a high hot work applicability in die casting, since one of the dominant failure mechanisms in die casting is heat checking [21].

Aside the results a short discussion on thermal fatigue testing will follow, there are four main comments on setup and procedure:

- Fatigue sample geometry are very long
- The inert gas shielding can be improved
- Sometimes temperature drift over time was observed
- Thermocouple measurements inside induction fields

The thermal fatigue specimen geometry is long. The heat affected zone is only one third of the whole length. The concentric $\varnothing 4\text{mm}$ internal cooling channel is difficult and expensive to machine. To decrease the experimental costs, shortening the sample length from 80mm to 55mm is therefore proposed. The poor process robustness of an $\varnothing 4\text{mm}$ drill with 20°D length to diameter ratio, compared to the more rigid and cheaper 15°D drill promotes this change.

Argon gas shielding was not sufficient to completely prohibit surface oxidation in the heat affected zone. By re-designing the Teflon bushings (balloon 2 & 3 in Figure 14), gas inlet pipe and the quartz-tube used to create the compartment for inert atmosphere, the oxidation can be prevented. This would be important for materials such as AM 1.2709 since heavy surface oxidation occurred during testing, possibly skewing results, since oxidation might act as stress rising nucleation points for fatigue cracking to occur [23, 21].

The temperature monitoring was made with thermocouples spot welded to the sample surface. In some instances, the temperature drifted over time e.g. reaching higher max temperature at higher number of elapsed cycles, than programmed in the first few heating cycles. Several factors could influence this behavior; the oxidation of the sample surface might change the electrical connection between thermocouple and sample, residue build-up inside the cooling channel might isolate and lower the cooling effect, and lastly, operating thermocouples inside electromagnetic fields might show unstable/un-calibrated temperatures. The induction coil might induce currents into the thermocouple leads, resulting in measurement errors as big as 10% reported by [39]. Calibration of the temperature measurement could lead to lower uncertainties in the thermal fatigue testing. One way is to use the laser speckle strain monitoring equipment available for the testing apparatus. This equipment needed substantial refurbishments, thus fell out of scope for use

in current investigations. Laser speckle strain measurements on the surface would increase the precision of the measurements, and enable easier comparison between results. This is simply due to the fact that it is the cyclic strain giving rise to thermal fatigue cracks, not the temperature itself that is the interesting testing parameter. It might have been the case that different materials in the test experienced different surface strain at the same temperature. This would in that case mean that the fatigue regimes might have been different, i.e. some samples experienced low cycle fatigue whilst others might experienced high cycle fatigue. Thus, the thermal fatigue test should also monitor surface strain in order to give as conclusive results in the same manner as the works done by Person 2003 [24] and Sjöström 2005 [25].

5.2 Static soldering

Results from static soldering are shown Figure 31 below. Each material (S1-S4) layer is represented with a curve. The filled in points are measured data points, and the curve in between was fitted to the theoretical parabolic intermetallic growth rate function proposed by [27]. The green curve for materials S2 (AM 1.2709) show a more aggressive growth rate than the other three materials. The blue curve (S1) for Uddeholm Orvar Supreme seems the most stable over time.

Static soldering intermetallic layer growth as function of time

Measured data points and fitted parabolic growth rate lines

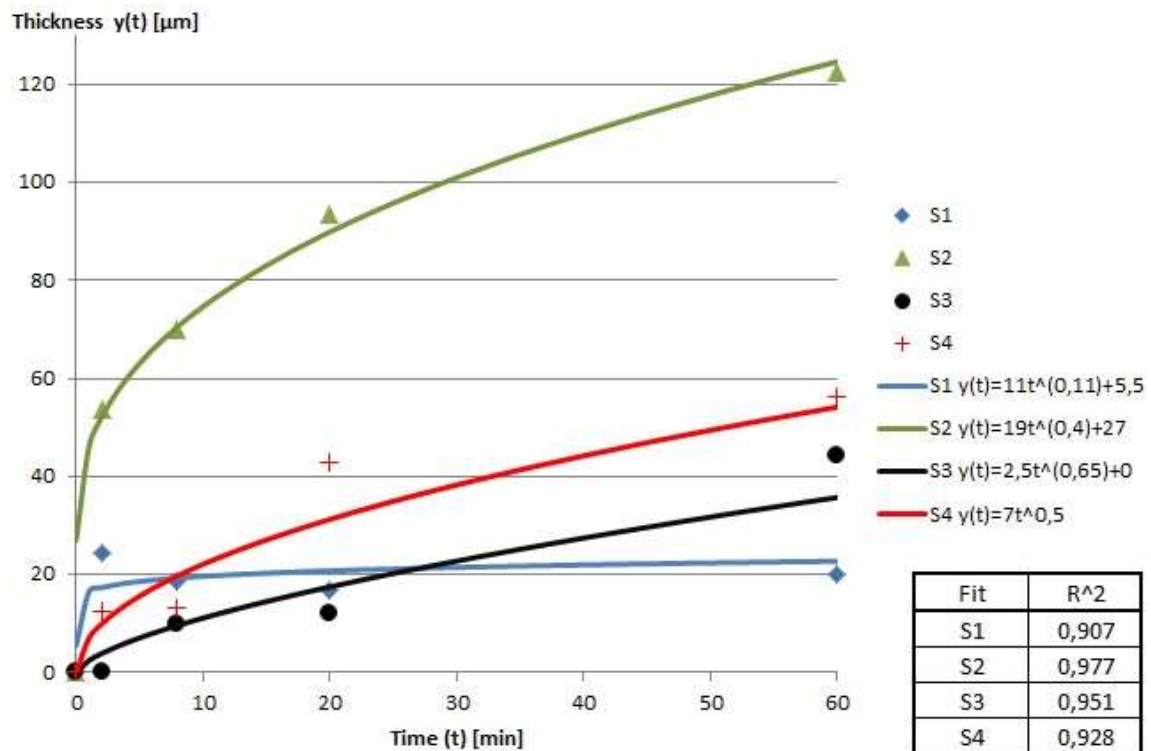


Figure 31. Intermetallic layer thickness as a function of time for the stationary soldering experiments. The legend shows which curve represent which material. Points are measured values, curves are fitted parabolic growth rate functions, the factor of determination R^2 for the fitting for each curve is shown next to the legend.

The experimental results shown in Figure 31 was then further analyzed. With help of the theoretical growth rate expression shown in Figure 9, the experimental data was fitted to this theoretical model in Excel. The result is presented in Table 13, where the material S1-S4 parameters are fitted to the theoretical layer growth model. With Excel a correlation calculation between theoretical and measured values were used to drive the Excel Solver function towards optimizing the parameters K , a and C as close to correlation=1 as possible. The theoretical model data were then regression analyzed in Excel, and the R^2 coefficient of determination for experimental and theoretical model parameter function were calculated. The expression describing the intermetallic growth rate behavior of the materials is shown in the rightmost column in the table.

Table 13. Regression analysis of theoretical intermetallic growth model parameters to the measured experimental result.

Coff.					$y(t)=Kt^a+C$
Sample	K	a	C	R^2	Equ.
S1	11	0,11	5,5	0,907	$y=11t^{(0,11)}+5,5$
S2	19	0,4	27	0,977	$y=19t^{(0,4)}+27$
S3	2,5	0,65	0	0,951	$y=2,5t^{(0,65)}+0$
S4	7	0,5	0	0,928	$y=7t^{(0,5)}+0$

The model coefficients K and t^a was then used in the weighting procedure of the experimental data. When K and t^a take on small values, the growth rate curve is showing a slow and stable layer growth indicating good resistance against forming intermetallic layers. Both parameters was used in the weighing, and the material with the smallest value got the lowest score (deemed good) and the material with largest parameter value got the largest score (deemed bad). The weighting in Table 14 shows how materials performed in static soldering.

Table 14. Static soldering weighting matrix. The parameters K and t^a are weighted. The total score is shown in the rightmost column. Uddeholm Orvar Supreme (S1) show highest resilience to soldering

ID	K	Score	Weight	S*W	t^a	Score	Weight	S*W	tot. Score
S1	11	3	3	9	0,11	1	1	1	10
S2	19	4	4	16	0,4	2	2	4	20
S3	2,5	1	1	1	0,65	4	4	16	17
S4	7	2	2	4	0,5	3	3	9	13

The rapid growth of the intermetallic layer most probably would give rise to high wear rates in die casting operation, since the soldering layer is one prominent wear mechanism, and need a certain thickness to cause severe wear [30].

Further analysis of the soldering layers was made with EDS-analysis in a Scanning Electron Microscope (SEM). Questions arose when observing the LOM images of the layers in Figure 28. The questions the further SEM investigations tried to answer are:

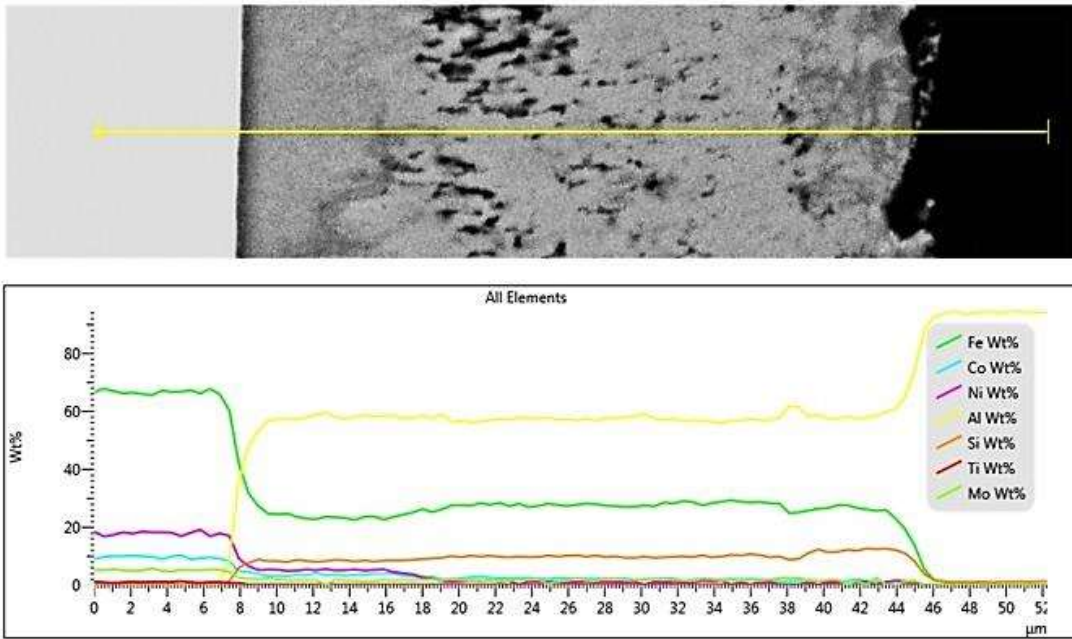
- 1) Is the Orvar Supreme and the AM H13 intermetallic layers the same at 2- and 60min?
- 2) Is AM 1.2709 intermetallic layer same as the hot work steel grades?

3) Is the region closest the substrate a very thin layer?

1). In Figure 33 a line scan EDS analysis of Orvar Supreme in a), and AM H13 in b) after 60 min is shown. The back scatter SEM image show a yellow line, along which the EDS line scan in the diagram below was taken. The diagram qualitatively shows how elements (see element legend) change in composition with distance.

The EDS analysis indicate that the composition along the line changes in the same manner for both Orvar Supreme and for AM H13. Iron decreases from bulk in two distinct steps. Aluminum and Silicon increases fast at the substrate border, and also show two distinct levels. This indicates that the two colored layers observed in LOM probably have different composition of intermetallic compound. The same behavior can be observed for Orvar Supreme, AM UAB1 and AM H13. Also in the back scatter image, elemental contrast between the two intermetallic regions indicates change in composition. In the two minute time interval, the single composition intermetallic layer also show very similar trends for the two hot work materials.

a) AM 1.2709 2min



b) AM 1.2709 60min

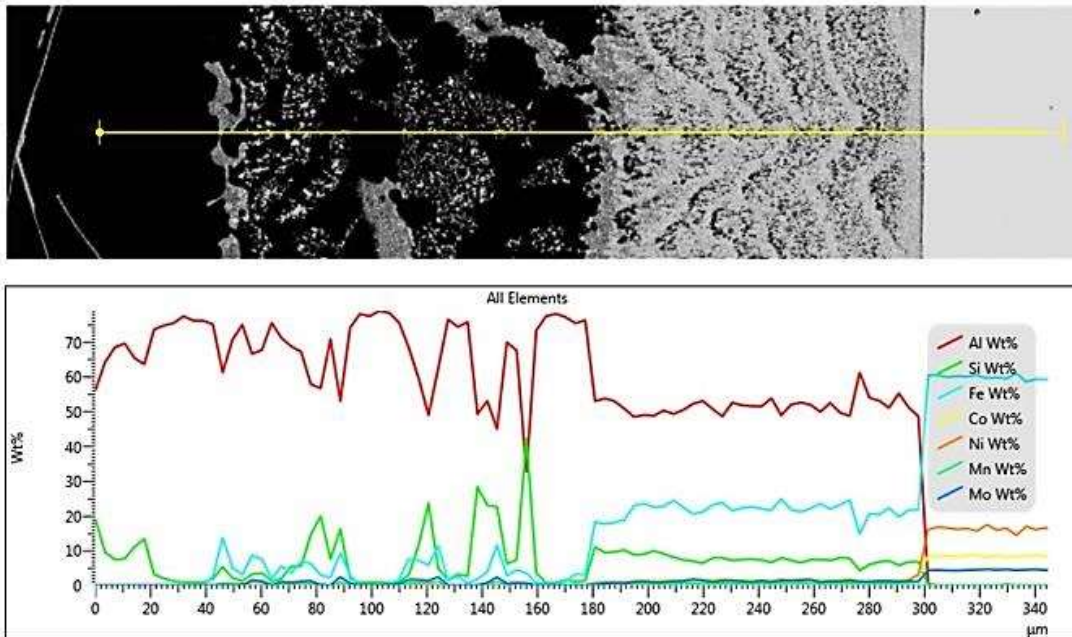
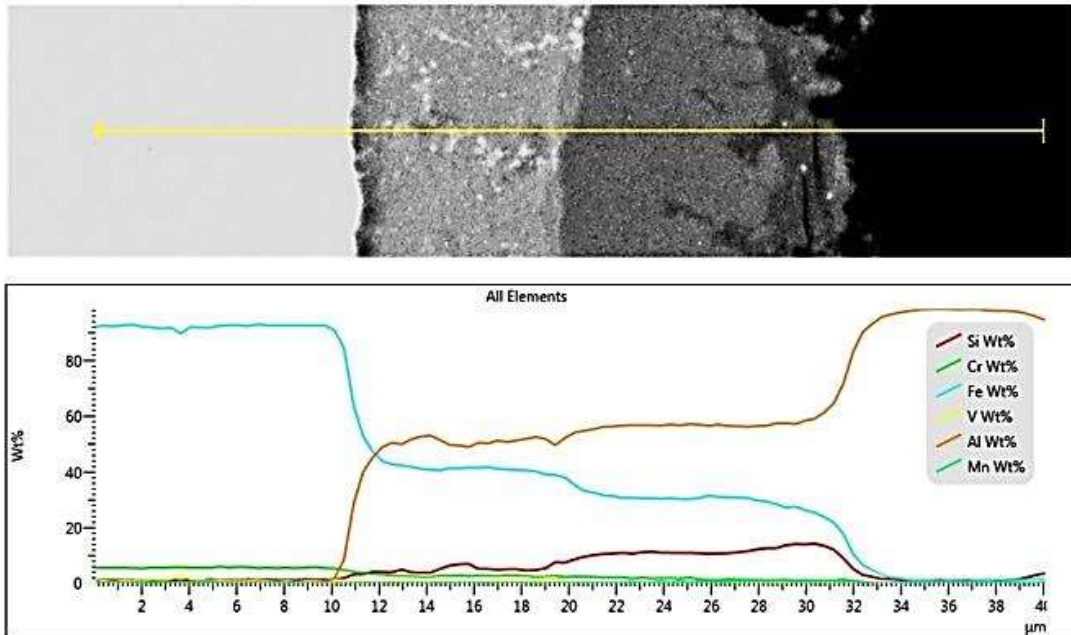


Figure 32. SEM EDS analysis of AM 1.2709 intermetallic layer. 2min shown in a) and 60min shown in b). Only one kind of intermetallic layer is observed, but with time segregation seem to appear.

a) Uddeholm Orvar Supreme, 60 min



b) AM H13, 60 min

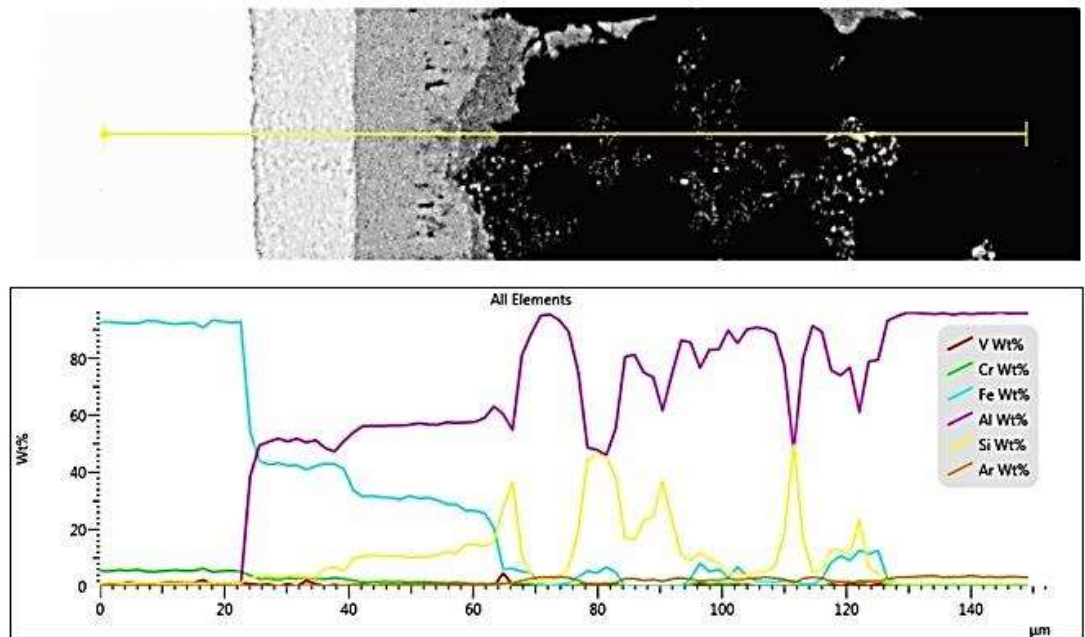


Figure 33. SEM EDS line scan images of 60 min soldering layers for Orvar Supreme in a), and AM H13 in b). The substrate steel is shown in the left side of the image, adhered aluminum in the right, and intermetallic layer in center.

The AM UAB 1 material did not show layers at 2min submersion. But after 60min, the two intermetallic layer, show very similar behavior to Orvar Supreme and AM H13. The line scan images for AM UAB 1 is omitted from the report, since no further interesting value would be added.

2) In Figure 32 the AM 1.2709 EDS line scans for 2min (a) and 60min (b) are shown. The 2min layer and the 60min layer show similar compositions, and aside the fact that the 60min layer is thicker than the 2min layer, when observing Fe-Al-Si layer, there is only one composition observed. Whereas in the hot work tool steel grades two distinct layers appear after that time. Please note that in b) the steel substrate is seen in the right side of the image.

Compared to the hot work tool steels mentioned above, the intermetallic region in AM 1.2709 also seems to mainly consist of Fe-Al-Si. If comparing the elemental levels of these species to the hot work layers, close resemblance can be seen. But one species only present in the AM 1.2709 is Nickel (see Table 5). The three hot work tool steels do not contain nickel. But [40] state that Ni/Al can form numerous intermetallic compositions. The conclusion is that the reactivity of the AM 1.2709 alloy might be influenced on the high nickel content. If nickel is bad for soldering resistance, that might very well explain the fact that the three hot work alloys don't have it in their composition.

Nickel is used in steels to increase the corrosion resistance, hardenability and to increase ductility and strength. But high hot hardness is reached by adding Cr, Mo, W, and V, and decreasing nickel according to [2]. The nickel content in the AM 1.2709 layers can be clearly seen in Figure 32, and in a) a distinct step is visible. The suspicion that the intermetallic composition differs compared to the hot work grade is even more encouraged by the fact. There is therefore logic to reason that the intermetallics formed in the AM 1.2709/ A380 couple have more rapid reaction kinetics, thus leading to worst resilience in soldering.

3) The region in between the substrate and the intermetallic layers showed a very slight color difference (only distinguishable through the LOM oculars) in the LOM investigations. Was this an ultra-thin layer, too small to observe in LOM was the question that arose. With the help of the more capable SEM investigations, the secondary electron detector image shown in Figure 34a), compared to back scatter phase contrast image in b) for AM H13 show this region at x2000 magnification. Based on these images and the EDS line scans for the surface, two sources are proposed for the observed phenomena; either the substrate/intermetallic layer border was rounded over in sample preparation, thus giving edge effects, or, the steep diffusion gradients in this zone seen in EDS, can give other

contrast than the intermetallic layer. Springer et.al 2011 [41] report intermetallic layer showing this white edge nearest the steel substrate. The authors report that this area is Fe-Al-Si η -phase. This is therefore the most plausible cause for the observed phenomenon.

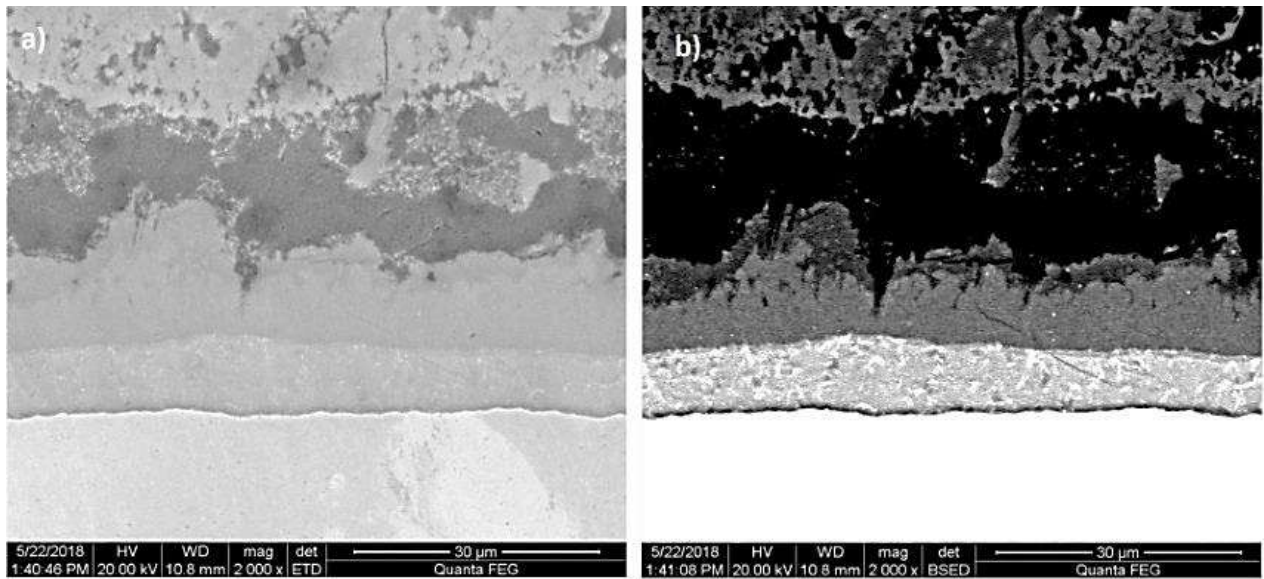


Figure 34. SEM images of AM H13 at x2000 magnification. Secondary electron detector in a), back scatter detector in b).

To conclude the discussion on the static soldering submersion experiments, the intermetallic layers observed are consisting of iron, silicon and aluminum in all materials. This means that the $Al_xFe_ySi_z$ combinations reported to exist by [27] in the H13/A380 couple probably was observed in this work. The exact combination of intermetallic phase was not determined in the scope of current work. This means that the statement that Fe_2Al_5 is fast growing [28], or that Al-Ni compounds might grow with more rapid growth kinetics cannot be determined. This hypothesis might explain the thick intermetallic layer and the fast wear rate of AM 1.2709, but cannot be determined here. Neither if the second layer that forms after longer interaction times are the slow growing Fe_2Al_2 [28]. The effect of different growth kinetics for different intermetallic compounds and the time it takes to reach a critical intermetallic layer that causes soldering damage to the tool [30] is still to be investigated. The observed difference between kinetics and layer formation between the three chemically similar hot work tool steel and the AM 1.2709, makes it interesting to discuss soldering resistance in a material engineering perspective. If the tool steel chemistry can be optimized (right composition and microstructure for hot work is paramount [2]); aiming for the slowest growing intermetallic layer in the tool steel/ aluminum couple towards maximal soldering

resistance. Or if alloy chemistry can lead to creating a diffusion barrier acting as a passive layer hindering soldering wear, much can be improved in today's die casting tool life. With the attractive attributes of AM-processing maybe some inherent mechanics, like fast solidification rate can open doors to exploring new interesting hot work alloys, not possible to produce with conventional melting practice.

It can be confirmed that the observed layers together grow parabolic, generally according to the theoretical growth rate expression given by [26]. For the Uddeholm Orvar Supreme and AM 1.2709 alloys a constant C , of 5,5 and 27 respectively is generated in the fitting process. This constant implies that at time zero, an initial intermetallic layer thickness $C \mu\text{m}$ exists. This is however impossible, since the samples have not been in previous contact with molten aluminum at time zero, thus cannot have an initial intermetallic layer. The exploration of this constant in these two materials maybe is of a mathematical nature. The theoretical parabolic growth equation proposed by the theorem [26] might not capture and describe the fast initial growth behavior observed for these two alloys. At the time interval between zero and 2 minutes elapsed time, the real growth kinetics are more rapid than what the model can describe, almost asymptotic for AM 1.2709, but in the model fitting procedure a close-to 1 correlation is generated when C takes on a value. The succeeding kinetics is well described for this two materials as well with the corresponding C -values. Strictly mathematically speaking, the C -value indicates a nominal intermetallic layer, but thus is rejected, and described as a mathematical artefact from the error in the model generated in the fastest growing interval close to time zero. The purposed growth rate equation might overestimate the influence of how the initial layer acts as a succeeding slower diffusion barrier hindering successive growth, or that several different intermetallic layers form in certain material couples and therefore altering the growth rate kinetics. The EDS-analysis for AM 1.2709 suggest a single layer, more detailed characterization and closer investigations could show how the growth rate kinetics behave close to time zero, this could then be used to see how the theorem from [26] differs from reality. This results in the need for closer experimental sampling frequency in the zero to two minute interval.

Other plausible explanations can also be discussed. Song et.al 2016 [42] suggest that the initial intermetallic growth reaction near the surface is governed by a non-diffusion process more similar to a linear model, than parabolic diffusion. Song et.al suggests that

intermetallic growth happens in two steps, one initial linear growth due to chemical reaction, and a succeeding diffusion process at later elapsed times. This could explain the behavior of AM 1.2709, that a linear expression at times close to zero succeeds the parabolic growth behavior. In order to conclude if this is the fact, more frequent sampled experiments near time zero is needed in order to see the eventual transition from a linear beginning to a parabolic evolution of the intermetallic layer.

A short discussion on the method in both static and agitated soldering will follow. In the tests, temperature of the molten aluminum fluctuated with $\pm 10^{\circ}\text{C}$ at 680°C temperature, corresponding to $\pm 1,5\%$. If using a larger melt, and a higher precision PID temperature controller, the melt temperature fluctuation might decrease, leading to more accurate results.

Specifically about static soldering method, it might be possible to perform them in a heat treatment furnace under protective atmosphere. Some dross and slag was formed on the surface of the melt pool during soldering, and during submerging of a new sample, some dross unavoidably adhered to the sample (even after careful manual removing of dross before the submerging). Urrutia et.al 2015 [40] conducted experiments with Nickel/Aluminum diffusion couple Transient Liquide Phase Bonding (TLPB) setup in protective gas atmosphere inside a conventional furnace. Tests with the similar approach is proposed in order to get better control of the soldering experiment. Another benefit would be that the aluminum in the couple is used only once. Degradation over time and repeated use would be avoided with the TLPD technique. For some sample materials, such as UAB 1 AM, oxide was quickly formed on the surface. The oxide prevented soldering in the 2min interval holding time for this alloy. This might be avoided by using a protective atmosphere oven for static soldering experiments. Since creating a diffusion barrier between the melt and the solid (i.e with an oxide layer or a coating) is one way to avoid soldering damage [24], preventing oxidization of the surfaces in testing is important in order to achieve valid results.

5.3 Agitated soldering

The results of the agitated wear is shown in Figure 30 was then weighted in the matrix in Table 15, lowest worn mass value gave the lowest score, and the largest wear rendered the material the greatest score. The weighing results show the most resilient material was

Uddeholm Orvar Supreme, and the least resistant material was AM 1.2709. Uddeholm Orvar Supreme got 1 point, and AM 1.2709 got 4 points.

Table 15. Agitated soldering total wear weighting matrix. Uddeholm Orvar supreme shows best resilience, AM 1.2709 suffered the biggest mass loss, hence has lowest resilience to agitated soldering wear of the tested alloys.

ID	Worn Mass [g]	Score	Weight	Total
A1	3,706	1	1	1
A2	6,394	4	4	16
A3	4,222	3	3	9
A4	3,932	2	2	4

Based on the behavior seen in the AM 1.2709 static soldering rapid layer growth, the significant mass loss seen in the agitated soldering and the very similar behavior of the three hot work tool steels, it seems as if AM 1.2709 composition gives low resistance to soldering wear. This makes the alloy unsuitable for use in die casting. This rapid behavior is also viewed as negative by [27], thus strengthening the statement that AM 1.2709 is unsuitable for die casting further.

For the hot work tool steel grades, the wear and material loss behavior is very similar, so without more data and higher precision in the experimental setup, they can be treated as equal, independent on the production process.

A short description of Pycnometry calculations will follow. The data presently presented in Figure 30, was calculated with the equations from the chapter about pycnometry metrology development. The equations were arranged in excel for easy processing of all experimental data. One spread sheet of this calculation for the A1 sample is shown in Figure 35.

A1

Parameter	Abr.	Value	Unit
Combined density	ρ^*	6,9844	[g/cm ³]
Combined Mass	m^*	89,7687	[g]
Combined Volumne	V^*	12,8527	[cm ³]
Initial mass steel	m_0	88,0236	[g]
Density Alu	ρ_a	2,7700	[g/cm ³]
Density steel	ρ_s	7,7440	[g/cm ³]
Concentration	K	15,2709	[% alu in steel]
Volume Steel	V_s	10,8900	[cm ³]
Mass steel	m_s	84,3319	[g]
worn Mass steel	WMs	-3,6917	[g]
Worn volume	Q	0,4767	[cm ³]

Volume STD	VSTD	0,0039	[cm ³]
Achieved dev.	A.Dev	0,0259	[%]

± from dev.

Worn volume	0,476712	-0,0033	[cm ³]
		0,0033	[cm ³]

Worn Mass	3,691656	-0,0256	[g]
		0,0256	[g]

Density correlation	1
---------------------	---

Figure 35. Excel spread sheet with pycnometry calculations for agitated soldering sample A1.

The spread sheet used to do the pycnometry evaluation for A1 agitated soldering experiment will be explained in detail. In the topmost area of the spread sheet, all the nominal parameters with abbreviation, value and unit is marked light blue. These cells are inputs used to calculate the green cells. The calculations follow the expressions given earlier in equations (7) - (9).

The combined density is measured with the pycnometer. Combined mass and initial mass are weighted on a precision balance before and after soldering. The density for A380 and the steel bulk samples were measured with pycnometry.

The concentration factor K , is used to calculate the worn mass and volume of steel, and by knowing the nominal mass of the sample, the mass change can easily be calculated.

From the pycnometry measurement two statistical values on the measurements are obtained (light blue cells). One is the Volume Standard Deviation for the measurement. This parameter is used to calculate the worn volume and worn mass error bars, as shown in blue cells. The other statistical error parameter called Achieved deviation, is the spread in pycnometry measurements. Each sample were run 15 times in the pycnometer, and the mean value of the best five runs giving the smallest Achieved deviation were used in the combined density measurements. The size of this spread is represented as Achieved Deviation.

To make sure that the calculation is valid, the cell called Density correlation is used. If the cell returns a value of 1, this means that the $(\text{Worn Mass}/\text{Worn Volume})/\text{Steel density} = 1$. This means that the both values show the same amount of wear in two different units. The calculation process was identically repeated for all the soldering samples.

When discussing agitated soldering, the velocity of the melt has to be mentioned. To simulate real erosion resistance of a hot work tool steel with impinging aluminum melt, higher velocity need to be reached, than what is possible with current setup. However, by using thinner samples, less stirring effect will occur in the melt. The “waves” on the aluminum melt surface, restricting higher rotational speed probably, will be lowered with thinner samples, thus enabling higher velocities. Also by reducing the level of the liquid height in the crucible, allows for more “careless” testing, since more waves in the crucible can occur before splashing out aluminum on the furnace top.

5.4 Validity and reproducibility

Thermal fatigue experiment setup is of accelerated life testing type. The validity of this approach may not be perfect when comparing alloys with big compositional differences. Also comparing results and data with different sources have proven tricky, since many use their own setup. But when comparing current results with earlier works not much can be said about reproducibility, since no one has tested additively manufactured materials in thermal fatigue before except [18], and that the strains measurements made by previous scholars could not be recreated in current work.

The validity of soldering as a simulation of die casting is also a topic for discussion. Since die casting molds often are pre-oxidized or coated, the diffusion will not occur as fast as in the current tests. This, however, is one step in isolating the soldering phenomenon, and understanding how the hot corrosion and soldering mechanisms work with the materials alone. The validity of the melt/steel interaction is hence a valid approach, especially when designing new alloys with high resistance to soldering.

On the note of reproducibility and robustness of testing, some comments on the experimental setup needs to be given. The reproducibility in different tests is hard to assess without data statistics from multiple runs. The many factors influencing on the reproducibility off course also influence precision of measurements. And in order to prove causality on the test variables influence on the test responses for the test materials, a structured Design-of-Experiments test matrix is needed. Since the current work was performed early in the evolvement of AM-feed stock powders, the price and lead time for samples resulted in a less stringent test plan, favoring testing general behavior for more alloys, than with high precision determining the precise properties of one alloy.

In agitated soldering, development of the pycnometry method is regarded as a contribution that can help others in future work. The gained analysis speed, the health- and environmental gains with pycnometry over NaOH-dissolution favors pycnometry. The precision with the method theoretically is high, but how high it can be in the actual case needs to be investigated further, since the dross formed on the surface of the aluminum melt have shown evidence of pores and blisters, and that the dross most likely have a different density than the A380 alloy itself. Closed porosity will lower the density of the adhered aluminum, thus giving a slight error in the measurements.

5.5 Future work

Isolating mechanisms and testing them individually is always an trade of from reality. The current work tried to simulate three isolated mechanisms in die casting of aluminum that normally interact. The only way to actually simulate real material loads during die casting, is to use a die casting machine, and try different alloys in the mould. This however is very expensive testing. There are still many things left to investigate before reaching the same technological readiness level for AM produced hot work tool steel compared to conventional. The mechanical behavior of thermal fatigue such as creep, hot hardness,

temper resistance and oxidation resilience stated by [20, 2, 23] as very important properties, and detailed microstructural investigations such as the work done by [25], must be done to understand the AM material response in hot work applications better, especially for thermal fatigue understanding.

Thermo-Calc and DICTRA are thermodynamic and diffusion simulation software is capable of doing interaction analysis on what happens in the intermetallic reaction. The software also could prove useful if one develops a soldering resistant alloy system. Experimental runs can be used to confirm theoretical simulations. The intermetallic layers formed, might be investigated with XRD or TEM for phase identification. The intermetallics seem similar in EDS, but without specialized equipment, phase determination cannot be done. This might give valuable insight into the fundamental soldering mechanism.

Fatigue and thermal fatigue are branches of the materials science requiring very good statistical data in order to give conclusive results. The current work did not provide that. In future work it is proposed that a proper DoE-experiment in thermal fatigue investigation of a conventional and an AM alloy is done. In mechanical fatigue porosity in AM materials is said to be a very influential factor, thus minimizing porosity in AM materials are needed. In thermal fatigue of AM materials, especially hot work tool steels, the most detrimental factor is not well understood. Future investigations are needed in order to know what parameter in an AM material to optimize for attaining the best thermal fatigue resistance possible. The AM material properties and the AM processing and parameters together with feed stock powder, are closely interlinked, thus a relevant future research topic.

6 Conclusions

Based on the experimental results in the current work, the following conclusions can be drawn:

Thermal Fatigue

- AM UAB 1 has best thermal fatigue properties with few and short cracks
- Uddeholm Orvar Supreme shows better thermal fatigue properties than AM H13, 1/3 of the number of thermal cracks and 1/5 of the total crack length
- AM 1.2709 has very many short cracks, and a total length of 2/3 of Orvar Supreme

- AM H13 showed the longest cracks, and most pronounced heat checking
- The porosity observed in the metallographic investigations of AM materials was largest in AM H13, and the least in AM UAB 1. AM 1.2709 was more dens than AM H13

Static soldering

- The static soldering intermetallic layer growth behavior fit the theoretical parabolic growth rate equations well
- After 120 min in stationary soldering, the AM 1.2709 alloy had a intermetallic layer more than twice as thick as AM UAB 1, and 4 times that of Orvar supreme and AM H13
- The intermetallic compounds in the layer most probably consist of different phases since the EDS line scans seem to have distinct levels of the detected elements, but no investigation can prove this in current scope of the work

Agitated soldering

- AM 1.2709 is not suited for die casting, since rapid intermetallic layer growth in static soldering was observed, and largest material loss were recorded in agitated soldering
- Both AM UAB 1 and Uddeholm Orvar Supreme show excellent die casting applicability, (in close agreement with [25, 24]) Thin intermetallic layers, and low soldering wear material loss
- AM 1.2709 wore 150% more than the three hot work tool steel grades
- Pycnometry successfully was used to record agitated soldering material wear loss
- Based on current investigations the conclusion that can be made is that with right chemistry, and right AM processing, conventional material Uddeholm Orvar Supreme still is better than AM H13. This also complies with the literature study results, showing that conventional material still is better than AM material in general.

7 Acknowledgements

I would like to extend my sincerest gratitude to the people and organizations enabling this master thesis work! It has been a very intriguing and interesting journey with a whole lot of exiting meetings, discussions, processes and experiments! Personally I've learnt very much, and also enjoyed the working process.

For providing test materials, production of test specimens and for providing a solid industrial knowledge basis, Uddeholms AB is greatly acknowledged. Thanks to Mr. C. Oikonomou for patient supervising and aiding with progressing the project.

Karlstad University provided test and evaluation equipment for the experimental tests, teaching me and helping me in the process. The academic and scientific guidance provided by Mr. Prof. P. Krakhmalev is greatly appreciated, as well as the fruitful cooperation with the staff of the materials science department.

Finally I'd like to direct my deepest gratitude towards my family and friends for encouraging me to pursue a M.Sc. degree in engineering. Your help and encouragement was, and always will be of the outmost importance to me.

Thanks everyone!

Henrik Andersson

Hagfors, July 2018

8 References

- [1] F. Bonollo et.al, "High-pressure die-casting: Contradictions and challenges," *The Minerals, Metals & Materials Society*, vol. 67, pp. 901-908, 2015.
- [2] B. Smoljan, "An analysis of relationships between behavior and microstructure constitution of hot work tool steel," *Materials and Manufacturing Processes*, vol. 24, pp. 786-790, 2009.
- [3] F. Klocke et.al., "State-of-the-art laser additive manufacturing for hot-work tool steels," *Procedia CIRP*, vol. 63, pp. 58-63, 2017.
- [4] U. Bertoli et.al, "On the limitations of volumetric energy density as a design parameter for selective laser melting," *ELSEVIER Materials and Design*, vol. 113, pp. 331-340, 2017.
- [5] I. Yadroitsev and I. Smurov, "Selective laser melting technology: from the single laser melted track stability to 3D parts of complex shape," *Physics Procedia*, vol. 5, pp. 551-560, 2010.
- [6] I. Anderson et.al, "Feedstock powder processing research needs for additive manufacturing development," *Current Opinion in Solid State and Materials Science*, vol. 22, pp. 8-15, 2018.
- [7] M. Mazur et.al, "SLM additive manufacture of H13 tool steel with conformal cooling and structural lattices," *Emerald Rapid Prototyping Journal*, pp. 504-518, 2015.
- [8] M. Mazur et.al., "Numerical and experimental evaluation of conformally cooled H13 steel injection mould manufactured with selective laser melting," *International Journal of Advanced Manufacturing Technology*, vol. 93, pp. 881-900, 2017.
- [9] R. Mertens et.al, "influence of powder bed preheating on microstructure and mechanical properties of H13 tool steel SLM parts," *Physics Procedia*, vol. 83, pp. 882-890, 2016.
- [10] J. Yan et.al., "Selective laser melting of H13: microstructure and residual stress," *Journal of Material Science*, vol. 52, pp. 12476-12485, 2017.
- [11] P. Laakso et.al., "Optimization and simulation of SLM process for high density H13 tool steel parts," *Physics Procedia*, vol. 83, pp. 26-35, 2016.
- [12] J. Safka et.al., "Structural properties of H13 tool steel parts produced with use of selective laser melting technology," *Journal of Physics: Conference Series*, vol. 709,

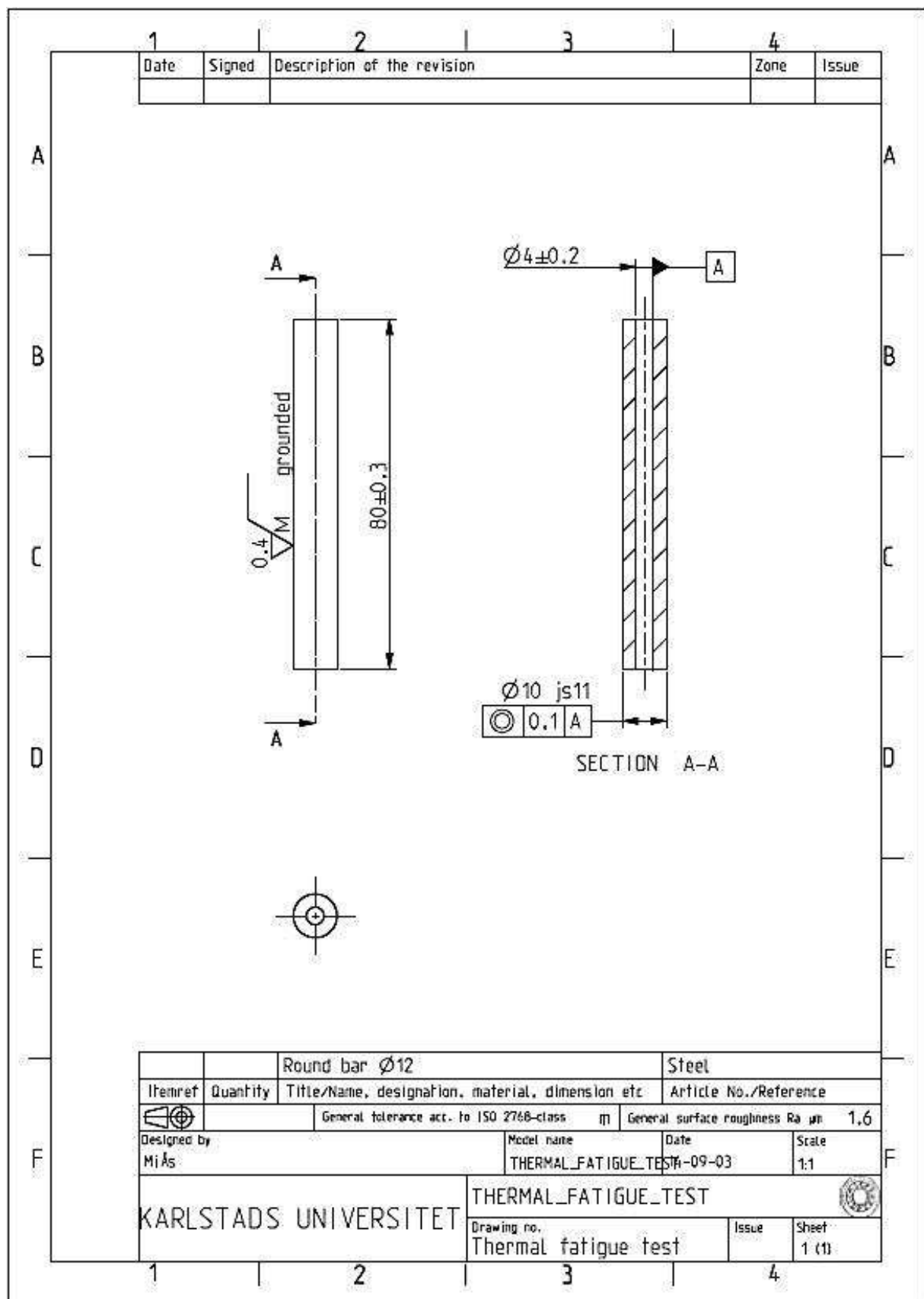
2016.

- [13] M. Holzwessig et.al, "Microstructural characterization and mechanical preformance of hot work tool steel processed by selective laser melting," *Metallurgical and Materials Transactions B*, vol. 46, no. B, 2015.
- [14] B. AlMangour, D. Grzesiak and J.-M. Yang, "Nanocrystalline TiC-reinforced H13 steel matrix nanocomposites fabricated by selective laser melting," *Materials and Design*, vol. 96, pp. 150-161, 2016.
- [15] Uddeholms AB, "Orvar Supreme," 01 05 2016. [Online]. Available: http://www.uddeholm.com/files/PB_orvar_supreme_english.pdf. [Accessed 20 12 2017].
- [16] F. Montevercchi et.al., "Cutting forces analysis in additive manufactured AISI H13 alloy," *Procedia CIRP*, vol. 46, pp. 476-479, 2016.
- [17] UDDEHOLM, "voestalpine-specialsteel.com," 13 12 2017. [Online]. Available: https://cms.aws-test.voestalpine-specialsteel.com/app/uploads/sites/43/2017/10/Skarande_bearbetning_1508.pdf. [Accessed 13 12 2017].
- [18] Y. e. Wang, "Thermal fatigue behaviour of an iron based sintered material," *Materials Science and Engineering A*, pp. 64-71, 2009.
- [19] J. Sjöström and J. Bergström, "Thermal fatigue in hot-working tools," *Scandinavian Journal of Metallurgy*, vol. 34, pp. 221-231, 2005.
- [20] R. Ebner et.al, "Thermal fatigue behaviour of hot work tool steels- Heat check nucleation and growth," in *7th international tooling conference*, 2006.
- [21] D. Klobcar et.al, "Thermo fatigue cracking of die casting dies," *Engineering Faliure Analysis*, vol. 20, pp. 43-53, 2012.
- [22] T. Dahlberg, *Teknisk Hållfasthetslära, Studentlitteratur*, 2010.
- [23] A. Weronski and T. Hejwowski, *Thermal fatigue of metals*, New York: Marcel Dekker, Inc., 1991.
- [24] A. Persson, *On tool failure in die casting*, Uppsala: Acta Universitatis Upsaliensis ISBN:91-554-5659-6 , 2003.
- [25] J. Sjöström, *Chromium martensitic hot-work tool steels- damage, performance and*

- microstructure, Karlstad: Karlstad University studies, ISBN:91-85335-21-5, 2004.
- [26] K. Nazari and S. Shabestari, "Effect of micro alloying elements on the interfacial reactions between molten aluminum alloy and tool steel," *Journal of Alloys and Compounds*, vol. 478, pp. 523-530, 2009.
 - [27] J. Joshi et.al, "Intermetallic formation and its relation to interface mass loss and tribology in die casting dies," *WEAR*, vol. 256, pp. 1232-1235, 2004.
 - [28] H. Shahverdi et.al, "Microstructural analysis of interfacial reaction between molten aluminum and solid iron," *Journal of Materials Processing Technology*, vol. 124, pp. 345-352, 2002.
 - [29] X. Li et.al, "The Al-rich part of the Fe-Al phase diagram," *Journal of Phase Equilibria and Diffusion*, vol. 37, no. 2, pp. 162-173, 2016.
 - [30] Q. Han and S. Vismanathan, "Analysis of the mechanism of die soldering in aluminum die casting," *Metalurgical and Materials Transactions A*, vol. 34, no. A, pp. 139-146, 2003.
 - [31] H. Xiaoxia et.al, "Effect of Si on the interaction between die casting die and aluminum alloy," *Materials Letters*, vol. 58, pp. 3424-3427, 2004.
 - [32] M. Mazar et.al, "Welding of aluminum alloys to steels: an overview," *International Journal for Manufacturing Science and Production*, vol. 14, no. 2, pp. 59-78, 2014.
 - [33] "MatWeb," 28 02 2018. [Online]. Available: <http://www.matweb.com/search/datasheet.aspx?matguid=e9f7cb19eb81450d8f67966151bd1802&ckck=1>. [Accessed 28 02 2018].
 - [34] S. Sievertsen, "Thermal Fatigue of tool steel," DiVA, diva2:944746 , 2016.
 - [35] Z. Chen and M. Jahedi, "Die erosion and its effect on soldering formation in high pressure die casting of aluminum alloys," *Materials and Design*, vol. 20, pp. 303-309, 1999.
 - [36] Y. Zhu et.al, "Evaluation of soldering, washout and thermal fatigue resistance of advanced metal materials for aluminum die-casting dies," *Materials Science and Engineering A*, vol. 379, pp. 420-431, 2004.
 - [37] M. Viana et.al, "About pycnometric density measurements," *Elsevier Talanta*, vol. 57, pp. 583-593, 2012.

- [38] H. Couto et.al, "Use of gas pycnometry for estimating the iron content in mineral samples," *Minerals Engineering*, vol. 39, pp. 45-47, 2012.
- [39] A. Smalcerz and R. Przylucki, "Impact of electromagnetic field upon temperature measurement in induction heated charges," *International Journal of Thermophysics*, vol. 34, pp. 667-679, 2013.
- [40] A. Urrutia et.al, "X-Ray characteriization of intermetallic phases in Al/Ni multilayer system," *Procedia Materials Science* , vol. 8, pp. 1150-1159, 2015.
- [41] H. Springer et.al, "On the formation and growth of intermetallic phases during interdiffusion between low-carbon steel and aluminum alloys," *Acta Materialia*, vol. 59, pp. 1586-1600, 2011.
- [42] J. Song et.al, "Evolution of intermetallic phases in soldering of the die casting of aluminum alloys," *Metallurgical and materials transactions A*, vol. 47, no. A, pp. 2609-2615, 2016.

Appendix 1 Thermal fatigue sample manufacturing drawing.



Appendix 2 Soldering sample manufacturing drawing, same drawing for both stationary and agitated soldering.

